KELVIN FORCE MICROSCOPY OF CARBON NANOTUBES

A Thesis

Submitted to the Faculty

of

Purdue University

by

Brian Walsh

In Partial Fulfillment of the

Requirements for the Degree

of

Master of Science

May 2000

To all those who have helped me along this long road.

ACKNOWLEDGMENTS

The research presented here is part of a larger work done in collaboration between the schools of chemical engineering, electrical and computer engineering and the physics department at Purdue University. It is through this collaboration that we have been able to collect the needed skills and equipment to proceed effectively. Special thanks needs to be given to Elton Graugnard and Pedro de Pablo, without their help this work would not have been possible. I would also like to thank Prof. David B. Janes, Prof. Ron Reifenberger, Prof. Ronald Andres, as well as graduate students Takhee Lee, Jia Liu, Stephen Howell, Scott Critterden, and the rest of the students in the Nanoscale Science group at Purdue University for their contributions during the past two years. Thanks to Dr. Roger Proksch and Prof. Dan Dahlberg for giving me ample opportunities as an undergraduate to see that physics is about more than just equations and problem sets. Finally I want to thank my mom, dad, and especially my fiancee for their tireless support during my stay at Purdue University.

TABLE OF CONTENTS

Page

LIST OF TABLES

LIST OF FIGURES

Figure Page

Figure Page

Figure Page

ABSTRACT

Walsh, Brian, M.S., Purdue University, May, 2000. Kelvin Force Microscopy of Carbon Nanotubes. Major Professor: David B. Janes.

Carbon nanotubes have recently been the focus of intensive study due to their unique electronic and structural properties. One area of interest is the electronic transport properties of a single carbon nanotube or a "rope" consisting of a small number of carbon nanotubes. In order to gain insight into the transport properties of nanotubes, an experimental study of the electronic transport in multi–walled carbon nanotubes using Kelvin force microscopy (KFM) has been preformed. The KFM is an adapatation of the atomic force microscope (AFM) that combines the high spatial resolution of an AFM with the high sensitivity to electrostatic potentials of the vibrating capacitor (Kelvin) method. The KFM has been used to measure the local electrostatic potential of several samples consisting of single ropes of ohmically contacted multi-walled carbon nanotubes. The observed behavior falls into to three classifications: i) broken nanotubes, ii) a localized potential drop that corresponds to a change of the morphology of the nanotube, iii) a linear potential drop along the length of the nanotube with localized potential drops at the contacts. Simple electrostatic models have been developed to aid in the interpretation of the electrostatic potential images obtained by the KFM.

1. INTRODUCTION

The field of nanoscale and molecular electronics has spurred great interest in the development and characterization of new materials to be used as elements of future device structures. Carbon nanotubes, first discovered by Iijima [5] while performing high resolution transmission electron microscopy (TEM), have attracted much attention from the scientific community for their unique structural and electronic properties. Due to their very small diameter (1 – 40 nm), long lengths (> 50 μm), and the possibility that they may be ballistic conductors, [6] a natural application of carbon nanotubes is a molecular wire. While fundamental studies of the electronic and structural properties continue, some groups are already demonstrating the use of carbon nanotubes as elements in device structures. [7] Other uses of carbon nanotubes are in nanolithography, [8] the measurement of etch morphology in semiconductors, [9] tips for both atomic force microscopy and scanning tunneling microscopy, [10] and carbon based electronics. [11] Commercial applications of carbon nanotubes are on the horizon. Samsung has demonstrated low–voltage field emission displays using mats of carbon nanotubes as emitters, and other groups are actively studying the use of carbon nanotubes for hydrogen storage for fuel cells.

Since this is a new material, fundamental work to understand the electronic structure of carbon nanotubes still needs to be done. During the last nine years, numerous studies of both theoretical electronic properties [12, 13, 14, 15, 16, 17], and experimental transport studies [3, 7, 18, 19, 20, 21, 22, 23] have provided insight into the electronic transport mechanisms of carbon nanotubes. However, because of the infancy of this field, many unanswered questions remain.

The focus of this work is on the electronic transport properties of carbon nanotubes. Specifically it seeks to answer the question: are multi–walled carbon nan-

otubes ballistic conductors? [6] The technique used in this study to address this question is Kelvin force microscopy (KFM). The KFM is an adaption of an atomic force microscope (AFM), which is sensitive to the electrostatic potential of a given structure. Because the KFM measurements were performed at room temperature, only two transport models will be considered: ballistic transport and diffusive transport. "Textbook" ballistic transport in an ideal conductor has an unique electrostatic potential signature far different than what is expected from diffusive transport. By ideal it is meant that ballistic transport occurs from one contact to the other. In order to perform this study a new method has been developed to place low resistance contacts onto the ends of single ropes of multi–walled carbon nanotubes. Consideration is also given to the non–idealities of the electrostatic potential measurement. The KFM method measures the electrostatic potential over a finite area, the details of which depend on the capacitive coupling between the probe and the surface. A simple model has been developed to understand this characteristic of the instrument and used to model its effects on the electrostatic potential measurement of multi-walled nanotubes.

This report details work performed to date, and provides analysis of experimental results. An outline is as follows: Chapter 2 gives a brief summary of the electronic and physical structure of carbon nanotubes. Attention is paid to the transport characteristics of multi–walled carbon nanotubes and their relation to how the electrostatic potential behaves under bias. Chapter 3 details the Kelvin probe method and presents results from a model used to study the non–idealities of the measurement technique. This model is applied to solutions of Laplace's equation corresponding to different transport mechanisms in multi–walled carbon nanotubes. Chapter 4 presents the sample fabrication method, and experimental results from the use of the KFM on the resulting samples. Three characteristic behaviors have been seen: i) broken multi–walled nanotube, i) a multi–walled nanotube with a localized electrostatic potential drop associated with a change in the structure of the multi–walled nanotube rope, ii) a multi–walled nanotube with a linear electrostatic potential drop with evidence of

contact resistance. If the electrostatic model of an ideal ballistic conductor is modified to account for the presence of defects in a ballistic multi–walled nanotube, this nanotube can be analyzed in terms of both ballistic and diffusive transport models. The based solely on the electrostatic potential data one cannot distinguish between ballistic and diffusive transport models. Proposals for enhancement to this measurement technique are presented in Chapter 5. Chapter 6 summarizes the results of this work.

2. CARBON NANOTUBES

The use of carbon fibers dates back to the late 19^{th} century with the need for a material with special structural properties. The first carbon fiber was prepared by Thomas A. Edison to provide a filament for an early version of a light bulb. [24] Growth in the study of carbon materials accelerated in the 1950's with the growing need for very light and strong materials for the aviation industry and the space program. Carbon fibers with very small diameters of less than 10 nm have been known to exist since about 1976. [25] However with the recent interest in C_{60}, more commonly known as "buckyballs", more systematic studies of carbon nanostructures were performed which led to the discovery of carbon nanotubes. [5, 24, 26]

2.1 Physical Structure of Carbon Nanotubes

A carbon nanotube (CNT) is a seamless cylindrical shell of carbon atoms formed by "rolling" a graphene sheet into a cylinder. This is schematically illustrated in Figure 2.1. A system has been developed to classify the structure of the nanotube based on two integers (n,m) and the hexagonal basis vectors of the graphite lattice. [24] Convention defines a CNT described by the indices (n,0) as a zigzag CNT, and an armchair CNT is described by the two indices (n,n). The hexagons in the zigzag and armchair CNT will form rings perpendicular to the tube axis, whereas the hexagons of any other CNTs will spiral around the tube axis. The tubes with spiraling hexagons are called chiral tubes.

Two types of nanotubes exist: single–walled nanotubes (SWNTs), and multi–walled nanotubes (MWNTs). A MWNT consists of a number of concentric shells of SWNTs. The diameter of SWNTs ranges from 0.7 nm to 2 nm. MWNTs have diameters of 2 to $\sim$ 50 nm depending on the number of shells. For both SWNTs and MWNTs the length of a single tube can exceed 50 μm. This length to diameter

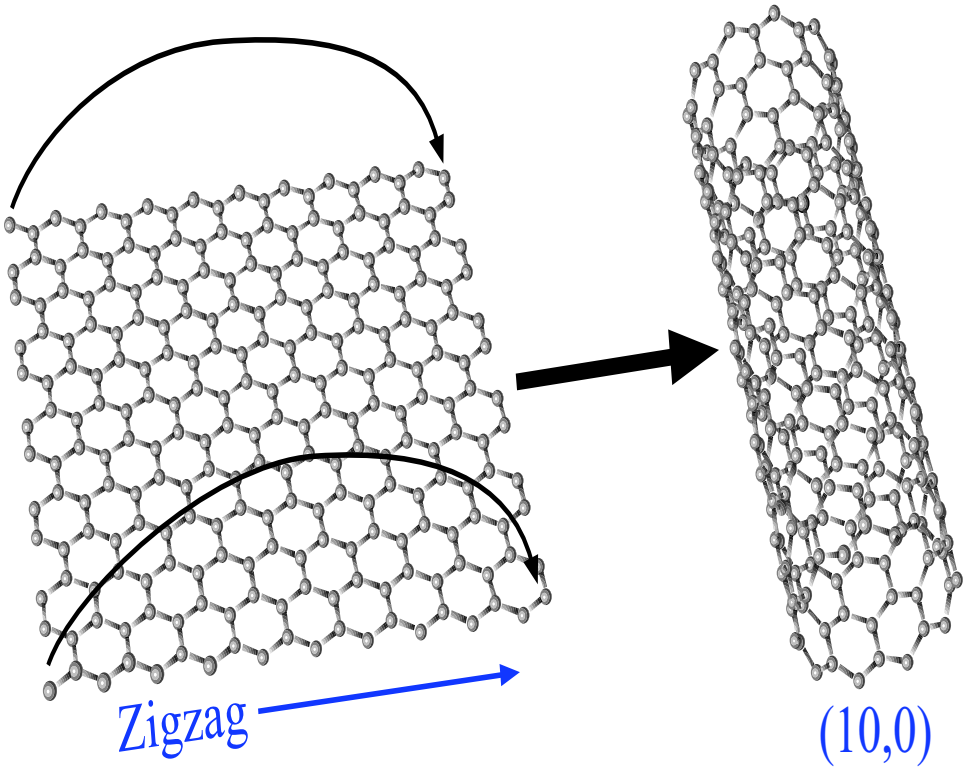

Fig. 2.1. Schematic representations of rolling up a graphene sheet to form a (10,0) zigzag single walled nanotube. Rolling the sheet in the direction perpendicular to the one shown above would produce a (6,6) armchair nanotube. [1]

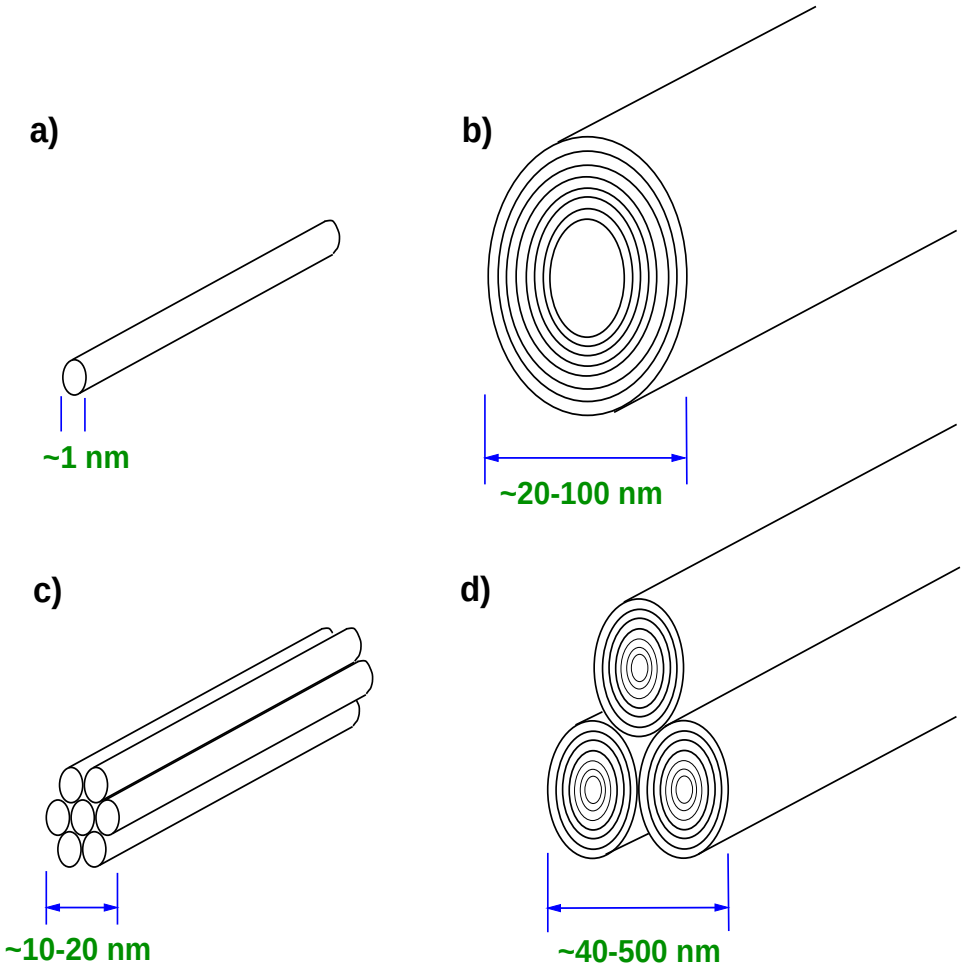

Fig. 2.2. Examples of single–walled nanotubes (SWNTs) and multi–walled nanotubes (MWNTs). a) An individual SWNT. b) An individual MWNT. c) A small bundle or rope of SWNTs, which may have hundreds of tubes. d) A bundle of a few MWNTs. [1]

ratio naturally suggests the use of carbon nanotubes as molecular wires or device interconnects. The differences between SWNTs and MWNTs are illustrated in Figure 2.2. In order to minimize surface energy, both SWNTs and MWNTs prefer to group into bundles of nanotubes that are called "nanotube ropes." The interlayer spacing in a multi–walled nanotube is ~ 0.34 nm, a value which has been confirmed by high–resolution TEM [5] and STM [27], and agrees closely with the average equilibrium value obtained from self–consistent electronic structure calculations. [28] It is believed that there is little structure correlation between the concentric tubes in a MWNT. [5, 29] That is, similar to turbostratic graphite, there is no ABAB stacking of the carbon atoms, and the chirality of the tube changes from layer to layer. In this study MWNTs were used exclusively. From atomic force microscopy data, in the samples that we used, the individual MWNTs are $5 - 20$ nm in diameter. The larger size of the MWNT facilitates handling, enabling us to manipulate single ropes of MWNTs. The MWNTs used in this study were grown using an arc-discharge method and generously provided by Dr. Richard Smalley at Rice University.

2.2 Electronic Structure

Due their simpler structure most of the theoretical work has been performed for SWNTs. Because of their size and atomic structure, SWNTs are expected to be 1D conductors and as such will exhibit interesting electronic transport properties. [6] Theoretical calculations of the electronic structure of MWNTs is complicated due to the presence of multiple shells of SWNTs. The effects of inter–shell interactions in MWNTs are unknown at this time.

The band structure of graphite can be calculated using tight binding theory, from which graphite is known to be a zero-bandgap semiconductor. [30] As shown in Figure 2.1, one could think of fabricating a carbon nanotube by rolling a single layer of graphite into a tube. Because of the small size of the resulting tubes, the electron states perpendicular to the axis of the tube are quantized. The resulting band structure is highly dependent on the diameter and chirality of the CNT. The band structure of CNTs shows both true metallic and semiconducting behavior with a

diameter dependent band gap. Examples of the band structure for a metallic and semiconducting tube are shown in Figure 2.3.

Other band structure calculations for nanotubes have been performed using a first principles local density-functional approach [6, 31], an empirical pseudo–potential method [31], and the Hückel tight-binding method. [6, 32, 33, 34, 35, 36, 37]

2.3 Transport Through Carbon Nanotubes

In order to interpret the results of the Kelvin force measurement a more thorough understanding of the structure of the MWNTs used in the study is needed. As seen from the band structure calculations, single shells of the MWNT can be either metallic or semiconducting. A MWNT is composed of multiple SWNTs each of which may have a different chirality and therefore a different band structure. Given an equal distribution of possible chiralities of nanotubes, statistically 1/3 of the nanotubes will be metallic while the remainder are semiconducting. The band gap of semiconducting nanotubes is given by: [38, 39]

$$E_{g-sc} = 2d_{nn}\gamma_0/D, \tag{2.1}$$

and the energy separation between the first sub–bands for a metallic nanotube is given by:

$$E_{g-m} = 3d_{nn}\gamma_0/D, \tag{2.2}$$

where d_{nn} is the C–C nearest bond distance (1.142 nm) and γ_0 is the $pp\pi$ hopping interaction (2.9 ± 0.2 eV). D is the diameter of the tube given by:

$$D = \sqrt{3}d_{nn}\sqrt{m^2 + mn + n^2}/\pi, \tag{2.3}$$

where n and m are integers describing the chirality of the MWNT.

Using these estimates of the band gap for semiconducting nanotubes Equation 2.1 shows that semiconducting nanotubes with a diameter less than 20 nm will not significantly contribute to transport at room temperature. The diameters of single MWNTs

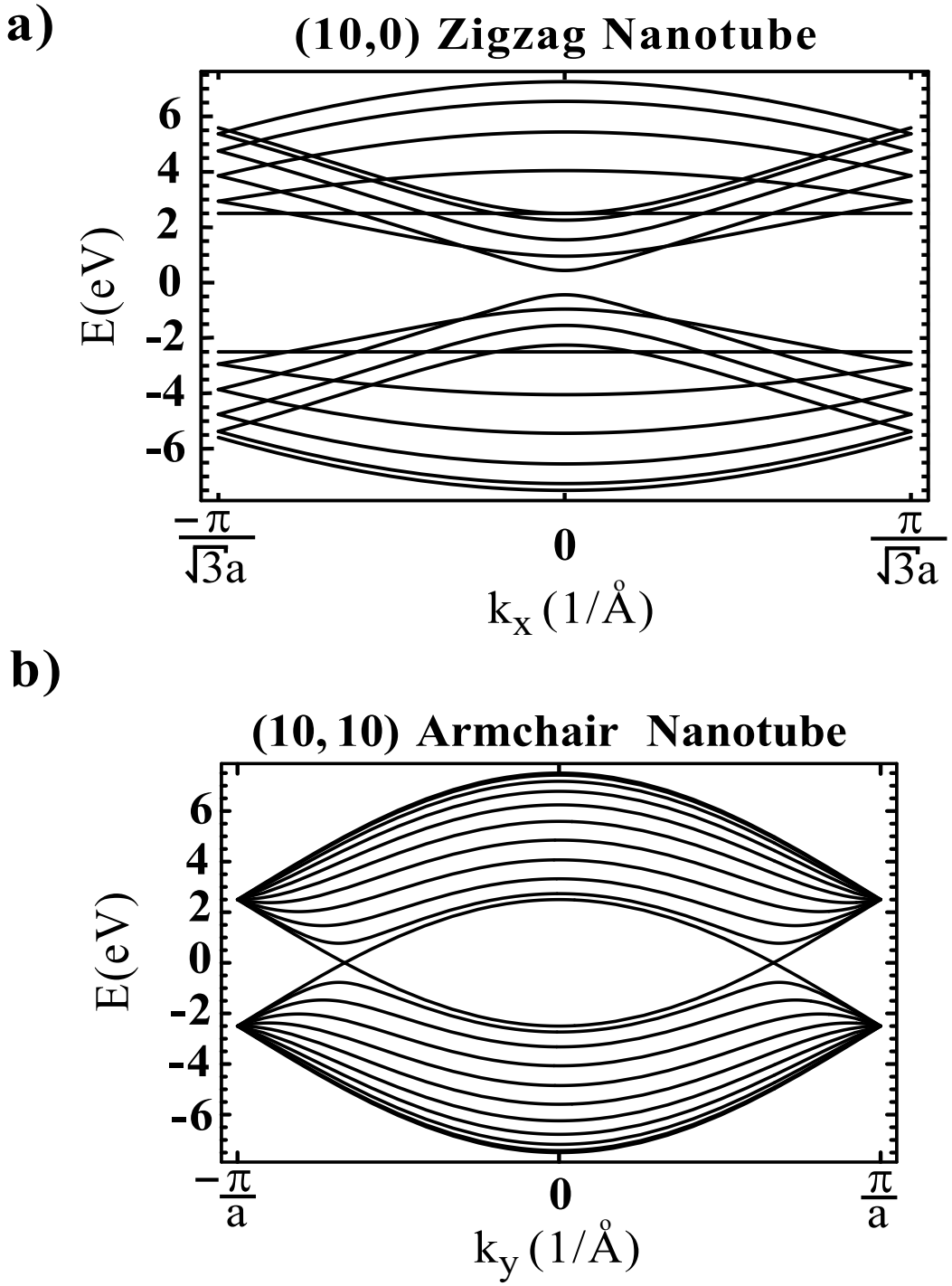

Fig. 2.3. Energy dispersion relations for two single walled nanotubes. The a) zigzag (10,0) nanotube and, b) armchair (10,10) nanotube. We see that the (10,10) is metallic and that the (10,0) nanotube is semi-conducting. [1]

as measured by atomic force microscopy (AFM) ranges from 5–20 nm. Therefore the transport through the MWNTs will be dominated by the metallic shells. Assuming a 1 nm minimum diameter, a 20 nm MWNT has a maximum of 28 shells. Based on sample dimensions and atomic force microscopy imaging (AFM), samples used in this study are ropes of MWNT containing 3 to 6 MWNT. Given that 2/3 of the shells are non-conducting at room temperature, we estimate that there are 28 – 56 metallic nanotubes available for conduction in an average sample. An unknown number of these nanotubes are either not continuous across the 4.2 μm distance between contacts, or not contacted by metallic contact pads.

For the continuous metallic shells connected to both contact pads, the transport mechanism still must be determined. Two of the proposed transport mechanisms in MWNTs are diffusive transport [40, 41], and ballistic transport.[2, 6, 20, 38] In what follows, we discuss these two models, their specific manifestations in MWNTs, and how they may be differentiated by use of Kelvin force microscopy.

2.3.1 Diffusive transport

One model for transport in carbon nanotubes is that the transport characteristics simply obey Ohms law. Intuitively, this is a reasonable model since these measurements are made at room temperature it is expected that phonon scattering and other thermally activated scatters will play a large role in the transport characteristics of MWNTs. Taking the limit of a many moded MWNT with enough scatters such that the characteristic scattering lengths are much less than the separation between the contacts, the MWNT can be treated as a classical ohmic conductor. The current is given as:

$$I = VG \qquad G = \frac{\sigma A}{L}, \tag{2.4}$$

where V is the applied bias, σ is the electrical conductivity, A is the cross-sectional area of the MWNT, and L is the distance between contacts. The conductivity of the sample will be determined by the experimentally measured relationship between the current flow, the applied electric field, and the sample dimensions. If we assume that

the resistance is dominated by the nanotube resistance (neglecting contact resistance), the above equations can be rewritten in terms of the electrostatic potential $\phi(x)$. We see that the electrostatic potential drop along the MWNT is linearly dependent on the distance away from the "high" contact.

$$\phi_{total} = IR = I\frac{L}{\sigma A} \qquad \phi(x) = I\frac{x}{\sigma A}, \qquad x \leq L \tag{2.5}$$

The electrostatic potential shown in Figure 2.4 is indicative of a resistive MWNT with a small amount of contact resistance. There is no condition that places any requirements on the measured resistance.

2.3.2 Ideal ballistic transport

It is thought that carbon nanotubes are the realization of a 1D ballistic conductor. By ideal it is meant that if electron scattering does occur inside a CNT, its effects on the scattering lengths are negligible. [38] Consider the case of an ideal MWNT connected to two electrodes as shown in Figure 2.5 (a). The nanotube will be ballistic if the mean free path of electrons in the system becomes much larger than the length of the nanotube. Even though the nanotube is ballistic, there is a resistance present in the system. In the contacts, the current is carried by many transverse conduction modes, but inside the nanotube, only a few conduction modes are available to carry current. A redistribution of the current in the contacts is required to inject current into the nanotube, resulting in a contact resistance. The contact resistance that results from this current redistribution will be called mode–matching resistance in order to differentiate it from other sources of contact resistance. The value for the mode–matching resistance is determined by the number of available conduction modes in the MWNT.

In the sample configuration of Figure 2.5 (a), if we assume that the contacts are reflectionless then the current as a function of bias is given by: [4, 42]

$$I = \frac{2e^2}{h} \sum_{i}^{N(\mu_1-\mu_2)} \tau_i(\mu_1 - \mu_2), \tag{2.6}$$

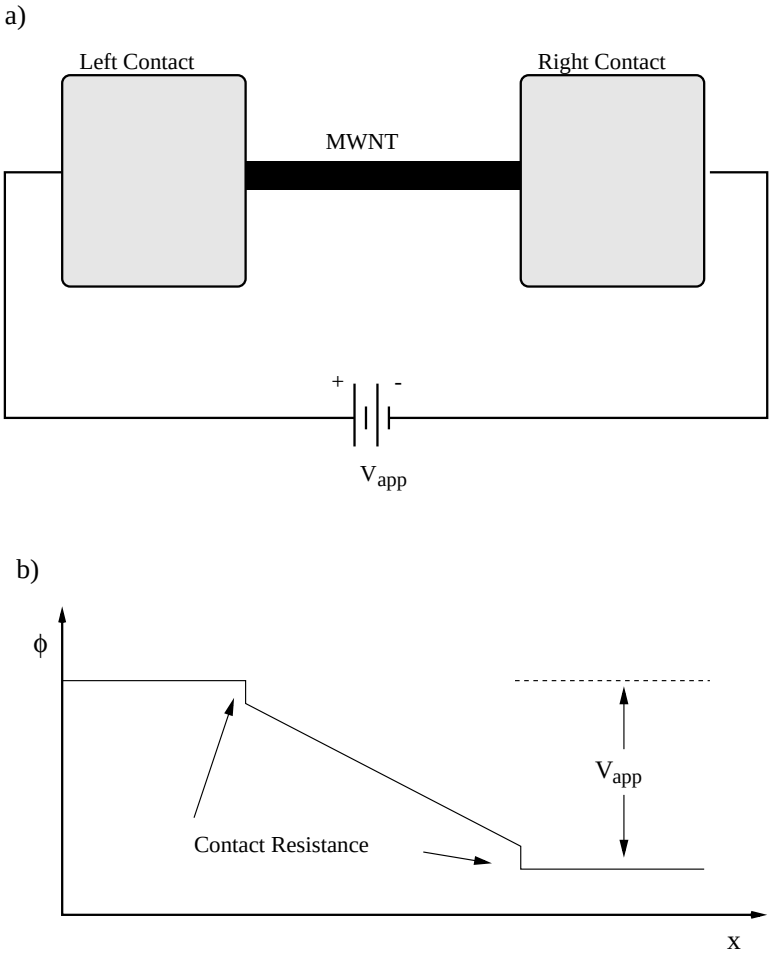

Fig. 2.4. a) MWNT connected by two wide contacts. b) The variation of the electrostatic potential (ϕ) across the nanotube assuming diffusive conduction and small contact resistances.

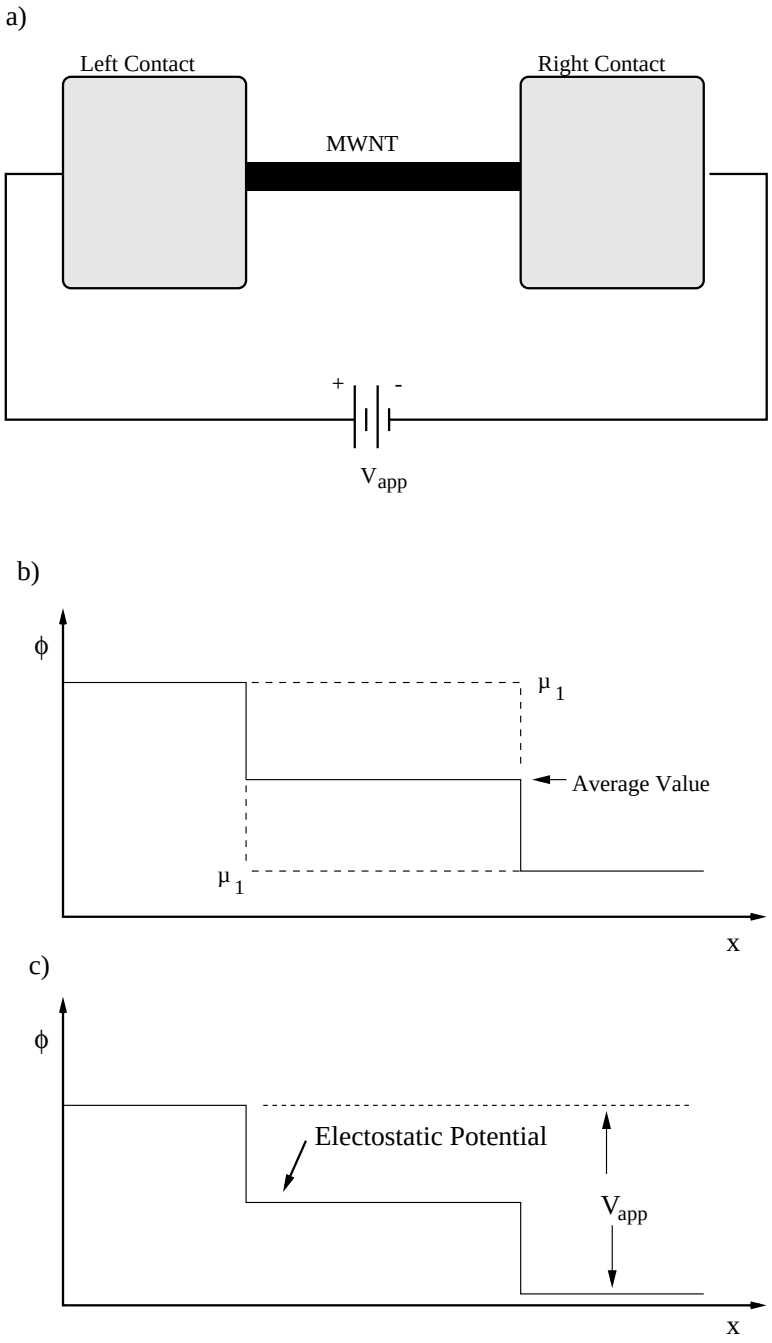

Fig. 2.5. a) MWNT connected by two wide contacts. b) The variation of the electrochemical potential (μ_1, μ_2) across an ideal MWNT. c) The variation of the electrostatic potential across the MWNT assuming no electron scattering.

where $N(\mu_1 - \mu_2)$ is the number of available conduction modes at a given voltage, μ_1 and μ_2 are the electrochemical potentials corresponding to the quasi–Fermi levels F^+ and F^- of the left and right contacts respectively. τ_i represents the average probability that an electron injected at one end of the conductor will transmit to the other end. This formulation assumes that τ_i does not depend on the energy of the electron.

If the nanotube is an ideal ballistic conductor ($\tau_i = 1$), the electrostatic potential follows the average quasi–Fermi level and is therefore dropped at each contact. The system resistance determined by the mode–matching resistance

$$G_c^{-1} = \frac{h}{2e^2 M} = G_0^{-1}/M, \tag{2.7}$$

where for a single metallic nanotube at low bias the number of conduction modes (M) is two. This would result in a system resistance of $1/2G_0$ or ~ 6.4 kΩ. Unfortunately, the number of conduction modes in the MWNT samples used in this study is unknown. Using the estimated number of conducting shells present in our samples, we expect a system resistance of 0.1 kΩ (112 conduction modes) to 12.9 kΩ (one conduction mode). If the MWNTs used in this study were defect free and had zero contact resistance, ballistic transport theory places restrictions on the measured conductance; it is expected that the conductance would be quantized in units of G_0/M. It is important to note that for this system the electrostatic potential will be equally dropped at each contact. This will lead to the "stair case" behavior of the electrostatic potential vs. position profiles as shown in Figure 2.5(c).

From an experimentalist's point of view, it is not unreasonable to assume that there is contact resistance from mode–matching as well as other scatters present at the interface between the disordered metal contact and a MWNT. For an ideal MWNT the addition of other scattering sources will not affect the behavior of the electrostatic potential drop along the MWNT. All of the electrostatic potential will still be dropped at the contacts. The amount of electrostatic potential drop at each contact will depend on the details of each MWNT–contact interface. Based on this

argument, the measured resistance values no longer need to be quantized in units of G_0/M. This makes it difficult to determine if conduction is ballistic based on measured resistance values alone.

2.4 Summary

Presented in this chapter was a brief introduction to the electronic and structural properties of carbon nanotubes as they relate to the electrostatic potential as measured by the Kelvin force microscopy technique. If the transport is diffusive, a linear electrostatic potential drop down the length of the conductor is expected. Depending on the details of the interface between the metallic contacts and the MWNT, some contact resistance may be seen. If the transport is ballistic, the electrostatic potential profile will show a stair case behavior; the electrostatic potential drop will be located in the contacts, and there will be no electrostatic potential drop along the length of the nanotube. This behavior is not dependent on any additional sources of contact resistance. If there is no additional contact resistance the conductance values will be quantized in units of G_0/M. However, the inclusion of an additional contact resistance will lower the conductance and remove the quantization condition.

3. KELVIN FORCE MICROSCOPY

From the work presented in the previous chapter, it is evident that there is a difference between the electrostatic potential profiles of diffusive and ballistic conductors. Ideal diffusive conductors will show a linear potential drop from one contact to the next; perfect ballistic conductors will only show contact resistance. By measuring the local electrostatic potential of a MWNT subjected to an applied bias, it may be possible to distinguish between transport mechanisms. The Kelvin force microscope (KFM) is an adaptation of the atomic force microscope (AFM) that is sensitive to electrostatic potential with millivolt sensitivity and ~ 100 nm lateral resolution. The KFM is based on the Kelvin probe method, a widely used technique to measure the electrostatic potential difference between two materials. Due to the long-range nature of the electrostatic force, the electrostatic potential detected by the KFM is distorted by the shape of the KFM probe as well as the morphology of the sample. A model has been developed that approximates the distortion caused by the finite sized cantilever tip and beam when used in the KFM measurement. Simple examples are presented to develop intuition about the behavior of this model. For the two transport models studied, the behavior of the electrostatic potential is known. Laplace's equation can be solved and then modified to account for the electrostatic potential convolution present in the KFM measurement.

For reference, a brief overview of the AFM measurement techniques is presented in Appendix 6.

3.1 Kelvin Probe Method

The vibrating capacitor method, or Kelvin method, is a well known technique for determining the contact potential difference between different materials. [43] In the Kelvin method, two conductors are arranged as a parallel plate capacitor with a

small spacing. In a simple model the contact potential between the two materials is $V_{CPD} = (1/e)(\Phi_1 - \Phi_2)$ where Φ_1 and Φ_2 are the work functions of the conductors. [44] A periodic oscillation of the distance between the two plates at frequency ω results in a current $i(t)$ given by

$$i(t) = V_{CPD}\omega\Delta C\cos(\omega t), \tag{3.1}$$

where ΔC is the change in capacitance due to the change in distance between the plates. For the measurement of the contact potential difference, an additional bucking voltage is applied between the plates and adjusted until the current $i(t)$ goes to zero. This method has high sensitivity to the contact potential difference between the plates, but the lateral resolution is limited by the size of the two conducting plates.

Higher lateral resolution can be obtained by using the Kelvin method in conjunction with an AFM. As described in Section 4.2 and Appendix 6, the AFM used in this study sequentially acquires the topographic data and the electrostatic data in two separate passes over the sample. During the second pass, only electrostatic forces are detected by the AFM. The electrostatic force on a conductive AFM cantilever held a distance z above a sample is given by

$$F = \frac{1}{2}\frac{\partial C}{\partial z}V^2, \tag{3.2}$$

where V is the potential difference between the cantilever and the surface of the sample, C is the capacitance between the cantilever and the sample. The potential is measured by using a null-force method. A voltage,

$$V_{tip} = V_{DC} + V_{AC}\sin(\omega_{res}t), \tag{3.3}$$

is applied to the cantilever, where ω_{res} is the mechanical resonance frequency of the cantilever. The resulting force on the cantilever is

$$F = \frac{1}{2}\frac{\partial C}{\partial z}[\phi(x,y) - V_{DC} + V_{AC}\sin(\omega_{res}t)]^2, \tag{3.4}$$

where $\phi(x,y)$ is the surface potential. This equation can be expanded to

$$F = \frac{1}{2}\frac{\partial C}{\partial z}[(\phi(x,y) - V_{DC})^2 + 2(\phi(x,y) - V_{DC})V_{AC}\sin(\omega_{res}t) + \frac{V_{AC}^2}{2}(1 - \cos(2\omega_{res}t))], \tag{3.5}$$

with spectral components at DC:

$$F_{DC} = \frac{1}{2}\frac{\partial C}{\partial z}[(\phi(x,y) - V_{DC})^2 + \frac{V_{AC}^2}{2}], \tag{3.6}$$

and at frequencies ω_{res} and $2\omega_{res}$:

$$F_{\omega} = \frac{\partial C}{\partial z}[(\phi(x,y) - V_{DC})V_{AC}], \tag{3.7}$$

$$F_{2\omega} = -\frac{1}{4}\frac{\partial C}{\partial z}(V_{AC})^2. \tag{3.8}$$

Using a lock-in amplifier, the F_{ω} component is used as the input to a feedback loop which adjusts V_{DC} to minimize F_{ω}. $F_{\omega} = 0$ when V_{DC} is equal to the surface potential $\phi(x,y)$ under the cantilever.

Ideally, the potential feedback loop will minimize the electrostatic forces on the cantilever resulting in an accurate measure of the surface potential $\phi(x,y)$. However, there are two effects which result in the modification of the measured electrostatic potential image: i) the topography of the surface, and ii) the shape of the AFM cantilever. The AFM cantilever is not a point probe; the capacitive coupling between all parts of the cantilever and the surface must be considered. The effective capacitance depends strongly on the shape and size of the tip as well as the size of the cantilever beam. The topography of the surface also changes the capacitive coupling between the cantilever and the sample. [45, 46, 47] In most KFM studies to date, these effects are neglected. The cantilever beam is several hundred microns long and $\sim 20\mu$m wide. As will be seen, the cantilever beam can play a large role in determining the electrostatic potential $\phi(x,y)$ measured by the KFM.

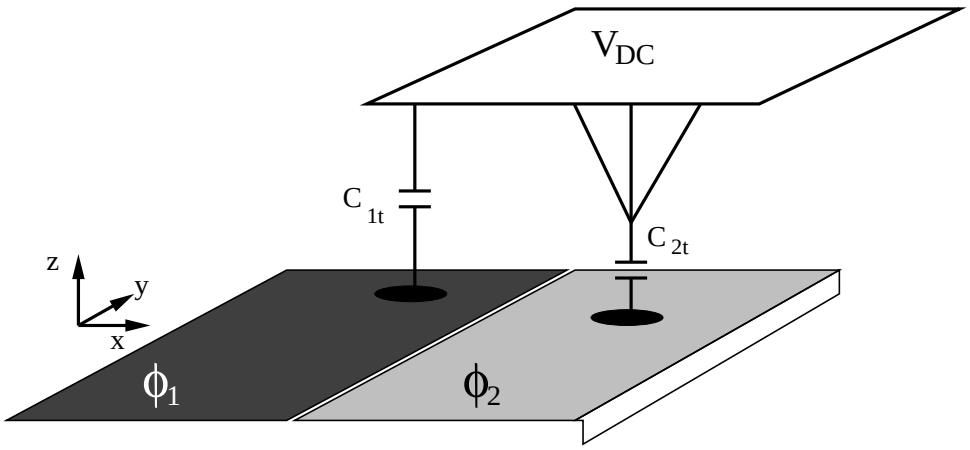

Fig. 3.1. A schematic of the distribution of the capacitive coupling from the tip to the surface. Because the tip is capacitively coupled to both electrostatic potential regions, the electrostatic potential will be sampled over both conductors.

Jacobs *et al.* have developed an elegant formulation for the effects of a finite sized tip on the potential image. [46, 48] Consider two regions with different surface potentials as shown in Figure 3.1. The attractive electrostatic force between the AFM cantilever and surface can be written as:

$$F = \frac{1}{2}C'_{1t}(\phi_1 - V_{tip})^2 + \frac{1}{2}C'_{2t}(\phi_2 - V_{tip})^2, \tag{3.9}$$

where C'_{1t} and C'_{2t} represent the derivatives of the cantilever–surface capacitance with respect to the separation distance. Setting $V_{tip} = V_{DC} + V_{AC}\sin(\omega_{res}t)$, the force F_ω on the cantilever is:

$$F_\omega = \frac{1}{2}C'_{1t}(\phi_1 - V_{DC})V_{AC} + \frac{1}{2}C'_{2t}(\phi_2 - V_{DC})V_{AC}. \tag{3.10}$$

The DC voltage required to zero the force on the tip is then given by:

$$V_{DC} = \frac{C'_{1t}\phi_1 + C'_{2t}\phi_2}{C'_{1t} + C'_{2t}}. \tag{3.11}$$

This can be generalized to an arbitrary number of capacitor plates (N) as:

$$V_{DC} = \frac{\sum_i^N C'_{it}\phi_i}{\sum_i^N C'_{it}}. \tag{3.12}$$

For a simple geometry of three plates each of width l as shown in Figure 3.2, Equation 3.12 can be evaluated analytically.

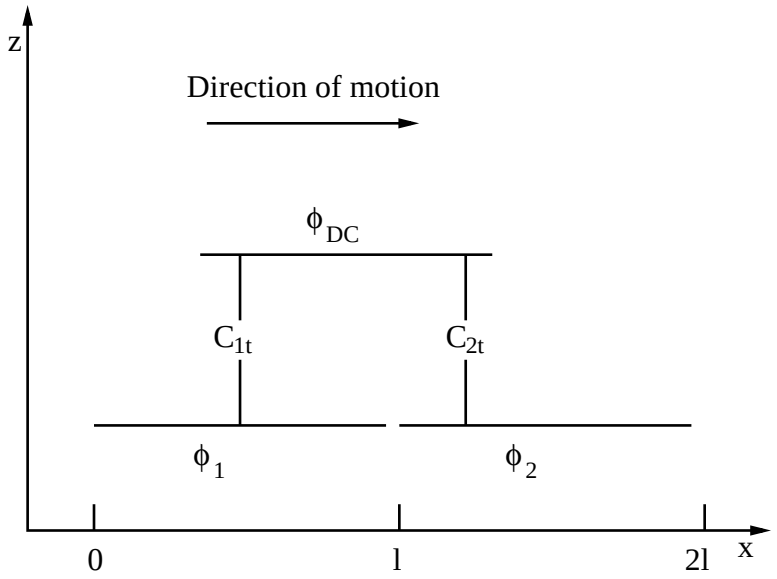

Fig. 3.2. Schematic of the model used to analytically solve Equation 3.11. As the top capacitor plate (length l) moves with respect to the two bottom capacitor plates, the capacitive couplings between the three plates vary. The strength of the capacitive coupling is directly proportional to the overlap area between the top plates and the bottom two plates. The potential measured by the KFM method is proportional to the relative strengths of the couplings.

Starting with Equation 3.11 and setting $\phi_1 = 0$ results in

$$V_{DC} = \frac{C'_{2t}\phi_2}{C'_{1t} + C'_{2t}}. \tag{3.13}$$

Substituting $C'_{1t} = -\epsilon_0 w(l-x)/z^2$ and $C'_{2t} = -\epsilon_0 w(x)/z^2$ and simplifying yields:

$$V_{DC}(x) = \frac{x}{l}\phi_2 \qquad 0 < x < l, \tag{3.14}$$

where l is the length of the capacitor plates. As the top capacitor plate is moved from $x = 0$ to $x = l$, a linear increase in the electrostatic potential will be recorded.

Physically, the linear increase in potential is due to the effect of a finite sized probe sampling the surface electrostatic potential of the two different regions. A further change will be seen if the surface or the tip is not flat, due to the non-uniformity of the dC/dz weighting factors. Such a geometry is difficult to study analytically.

To understand the measured electrostatic potential vs. position profiles, the relationship between the cantilever/sample geometry and the capacitive weighting terms $\partial C/\partial z$ must be examined. The magnitude of $\partial C/\partial z$ is approximately inversely proportional to the square of the separation distance. As seen in Figure 3.3 AFM cantilevers are composed of a pyramidal tip located on the end of a ~ 225 μm long and ~ 20 μm wide beam. During the KFM measurement, the very end of the pyramidal tip is held a small distance away from the surface ($\sim 15 - 25$ nm). The capacitive coupling between the end of the tip and the surface is very high, but the area of the tip is very small. Conversely, the capacitive coupling between the beam and the surface is very small, but the area is quite large. As shown in Equation 3.12, the potential measured by the KFM is a sum of any surface potential located under the cantilever with the contribution to the sum depending on the strength of the capacitive coupling.

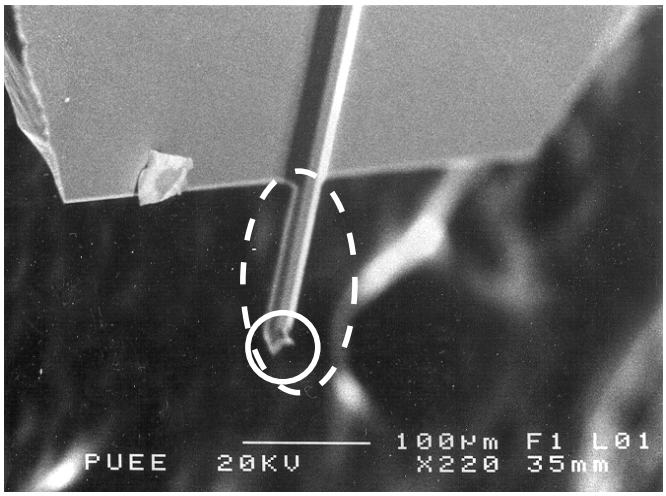

Fig. 3.3. SEM image of AFM cantilever showing the tip (solid circle) mounted on the beam (dashed oval) of the cantilever

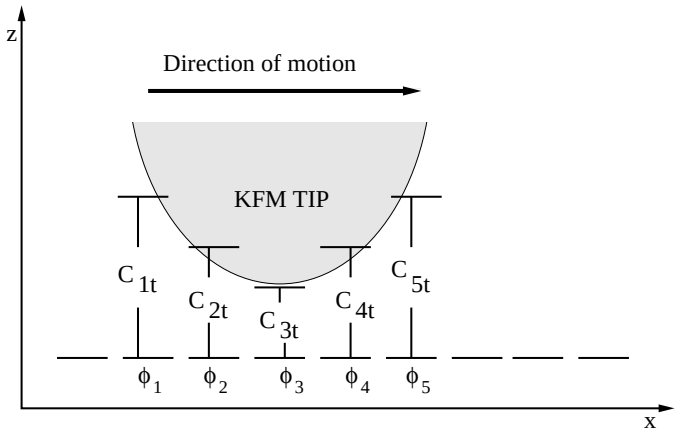

Fig. 3.4. A schematic for the tip/sample model used in this simulation. Both the tip and the surface are broken up into a series of parallel plate capacitors. The potential of each capacitor plate that defines the surface is independently set. Every capacitor plate that represents the KFM cantilever is at the same potential V_{DC}.

In order to visualize the consequences of this formalism with more realistic geometries, a program has been written and is included in Appendix A.1.4. As shown in Figure 3.4, the program breaks up the tip–sample geometry into a series of parallel plate capacitors. The capacitance ($C \propto 1/z$) and the derivative of the capacitance ($\partial C/\partial z \propto 1/z^2$) are calculated as a function of position of the cantilever with respect to the surface. This method for calculating capacitance will be referred to as the analytical method. For the simulations presented, the cantilever was modeled in three dimensions (XYZ) using a matrix of 100 x 100 elements, with each element representing a 35 x 35 nm capacitor plate. The sample was modeled in two dimensions (XY) by a 400 x 400 matrix with each element representing a 35 x 35 nm capacitor plate.

The method used in this program to calculate the capacitance is only valid when the width and length of the capacitor plates are much larger than their separation. This condition is not met for the bulk of the capacitor elements in this program. In order to evaluate the validity of the method used to calculate the capacitance in this

program, the capacitance vs. plate separation and $\partial C/\partial z$ vs. separation are calculated using a different method (method of moments) that correctly calculates the capacitance when the capacitor plates are spaced far apart. [49] A comparison between these two methods of calculating the capacitance for a parallel plate capacitor are plotted in Figures 3.5(a) and (b). As shown in 3.5(a), the value of the capacitance as calculated by the analytical method ($C \propto 1/z$) is much different than the capacitance calculated by the method of moments calculation. This is a result of the neglection of the fringing fields in the analytical capacitance method. However as shown in 3.5(b) the values for $\partial C/\partial z$ calculated by the analytical capacitance method are reasonably close to those calculated using the method of moments calculation.

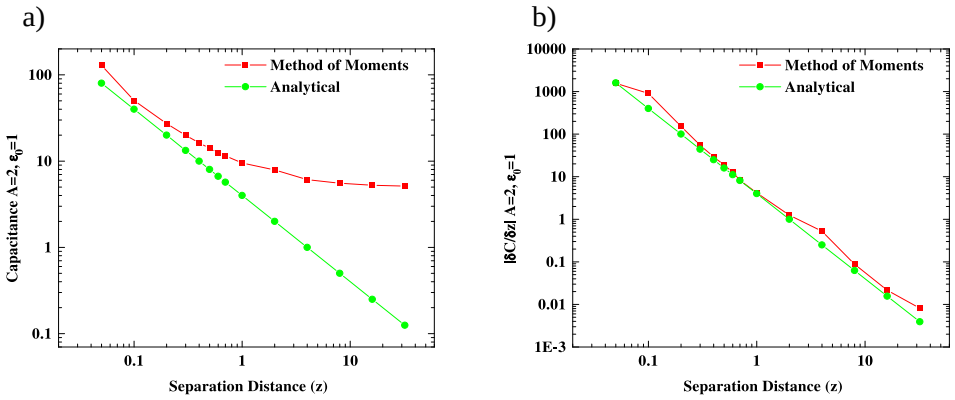

Fig. 3.5. A comparison between the calculated capacitance and $\partial C/\partial z$ using an analytical ($\sim 1/z^2$)calculation, and method of moments capacitance calculation for a parallel plate capacitor. (a) Capacitance vs. plate separation, (b) $\partial C/\partial z$ vs. plate separation.

This program has been used to investigate several aspects of the spatial resolution of the electrostatic potential with the KFM. The structure of the cantilever and sample can be varied from within this program. For all simulations shown, the tip is a pyramid of variable half–angle θ as defined in Figure 3.6. Around the tip is a $\sim 1\mu$m flat area representing the cantilever beam as seen in Figure 3.7. Table 3.1 lists the dimensions of the cantilever tip for a given half–angle. The cantilever is rastered across a specified potential and Equation 3.12 is evaluated. The simulations

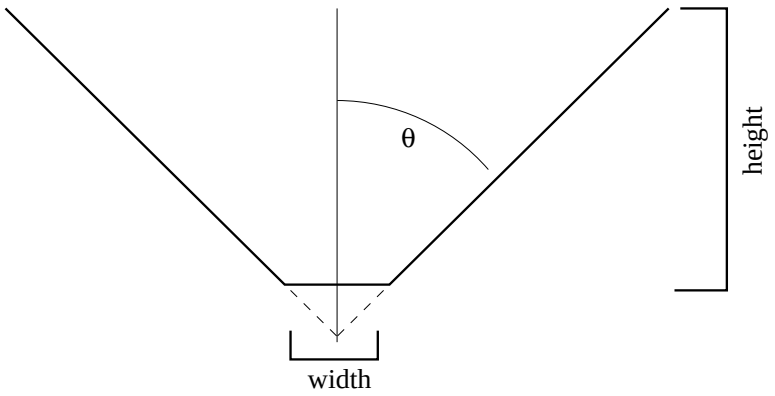

Fig. 3.6. Schematic of parameters used to define the tip of the cantilever. The half angle θ, the height and width of the tip are defined as shown.

Table 3.1
Tip height vs. half–angle for the tip geometries used in this study. The width of the end of the tip is 35 nm and the width of the base of the tip is 1.1 μm.

Half–Angle θ	Tip Height
45°	1.4 μm
26°	2.8 μm
18°	4.2 μm
14°	5.5 μm
11°	6.8 μm

are performed in 2D (XY), and electrostatic potential vs. position profiles are then taken.

Two test structures are used to demonstrate the electrostatic potential convolution effects of the KFM. The first test structure considered is a potential step where ϕ_s changes abruptly from 500 mV to 0 mV. Electrostatic potential vs. position profiles as a function of tip half–angle are shown in Figure 3.8 for this test structure.

As is seen in Figure 3.8 the electrostatic potential measured by the KFM is distorted from the specified electrostatic potential step by the geometry of the tip. Tips with a smaller half–angle θ minimize this distortion.

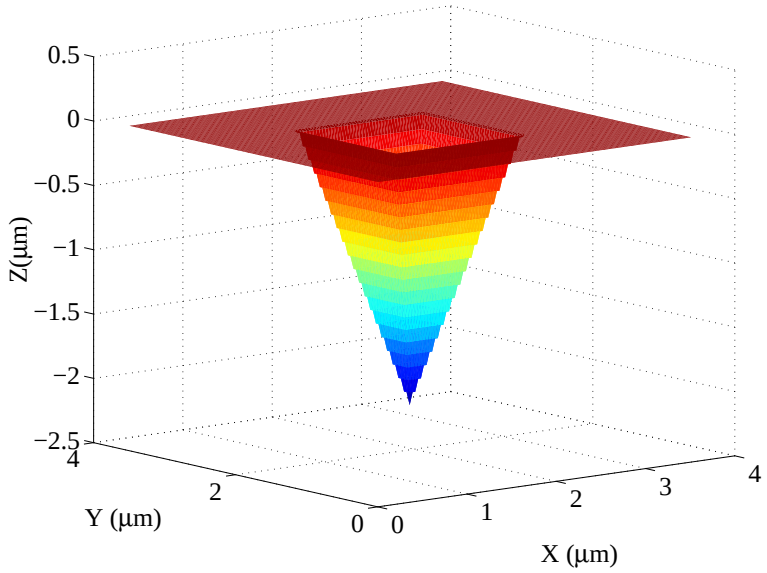

Fig. 3.7. An image of a simulated cantilever with a 18° tip half–angle and a $\sim 1\mu$m flat area at $Z = 0$ surrounding all four sides of the tip representing the cantilever beam.

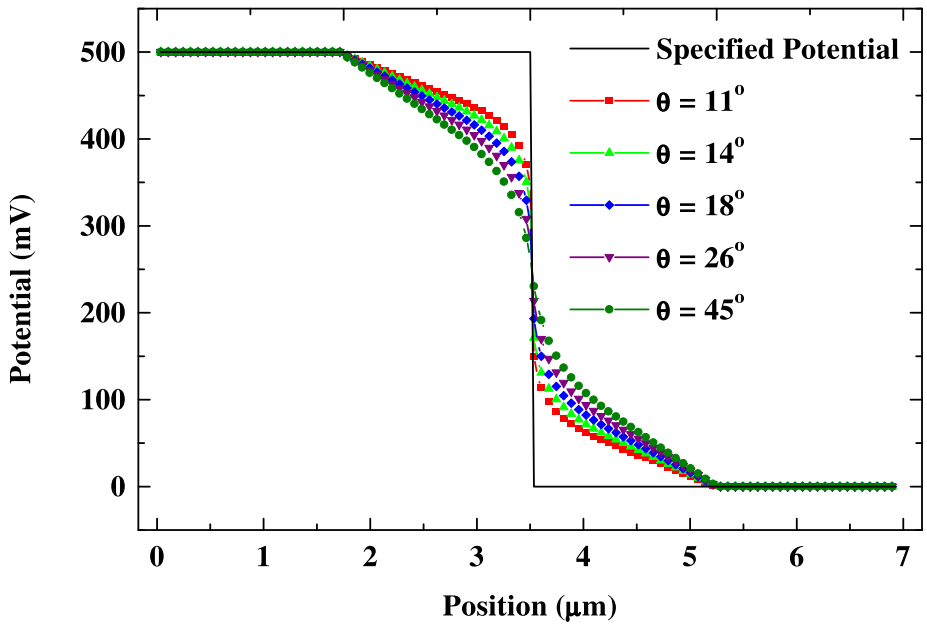

Fig. 3.8. Voltage vs. position profiles over an abrupt change in the potential from 500 V to 0 mV. The half–angle of the cantilever is varied from 11° to 45°. All profiles are taken at a distance of $\sim$ 35 nm from the surface. A representative image of the tip structure is shown in Figure 3.7

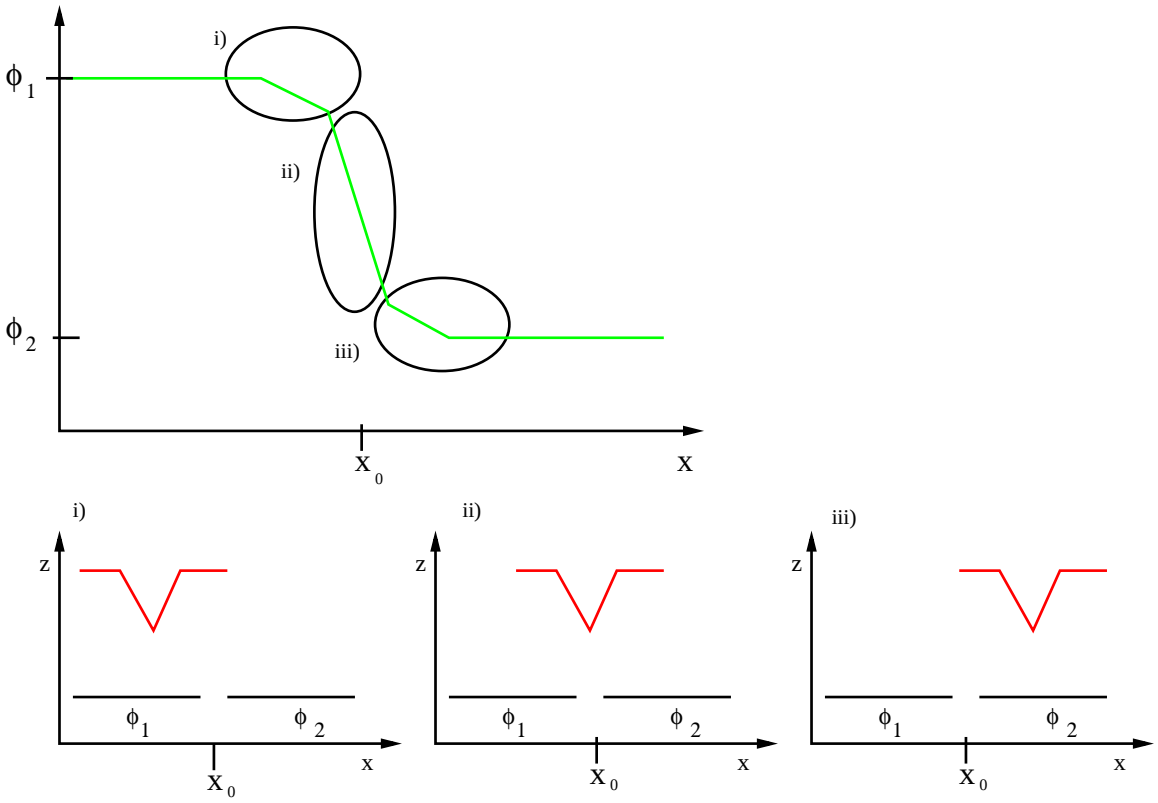

Fig. 3.9. Voltage vs. position profiles over an abrupt change in the potential from ϕ_1 to ϕ_2.

The electrostatic potential vs. position can be understood by breaking the profile up into three sections as seen in Figure 3.9. In region i), the small linear drop of the measured potential is caused by the cantilever beam being positioned over both potentials ϕ_1 and ϕ_2. While the cantilever tip is still located over the potential ϕ_1, the measured electrostatic potential deviates only slightly from ϕ_1. As the tip passes over the step in potential, the measured electrostatic potential changes quickly from ϕ_1 to ϕ_2 (region ii). The steepness of the transition is evidence that the tip plays the dominant role in localizing the measured electrostatic potential. As the tip moves away from the potential step, the area of the cantilever beam that is over the potential ϕ_1 is decreasing, resulting in a linear potential vs. position slope until (region iii) the entire cantilever is over the potential ϕ_2.

The response of the KFM to an electrostatic potential feature much smaller than the tip/beam system is also modeled. As seen in Figure 3.10 a 150 nm potential dot is specified. Again the electrostatic potential measured by the KFM as a function of tip half–angle is plotted. Tips with high aspect ratios (small half–angles) provide the most accurate measurement of the electrostatic potential, but even with the 11° tip, the measured potential is 2/5 the specified potential.

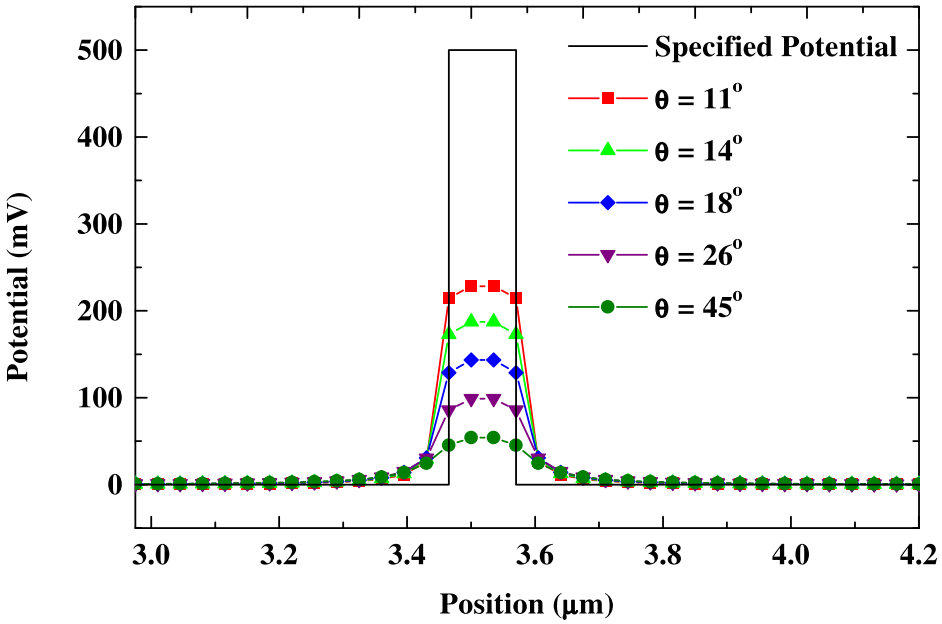

Fig. 3.10. Voltage vs. position profiles over a 150 nm wide 500 mV potential "dot". The half–angle of the cantilever is varied from 11° to 45°. All profiles are taken at a distance of $\sim$ 35 nm from the surface.

The capacitive coupling of the tip to the surface is inversely proportional to the tip-sample separation distance, which is expected to have a large influence on the measured potential. As seen in Figure 3.11, minimizing the tip-sample separation distance is critical to obtaining accurate potential measurements. As the tip-sample separation distance is increased, the effects of the strong local capacitive coupling between the tip and the sample are reduced.

The tip of the AFM cantilever wears over time. Figure 3.12 are SEM and TEM images of a new and used cantilever. The end-form of the tip also plays an important

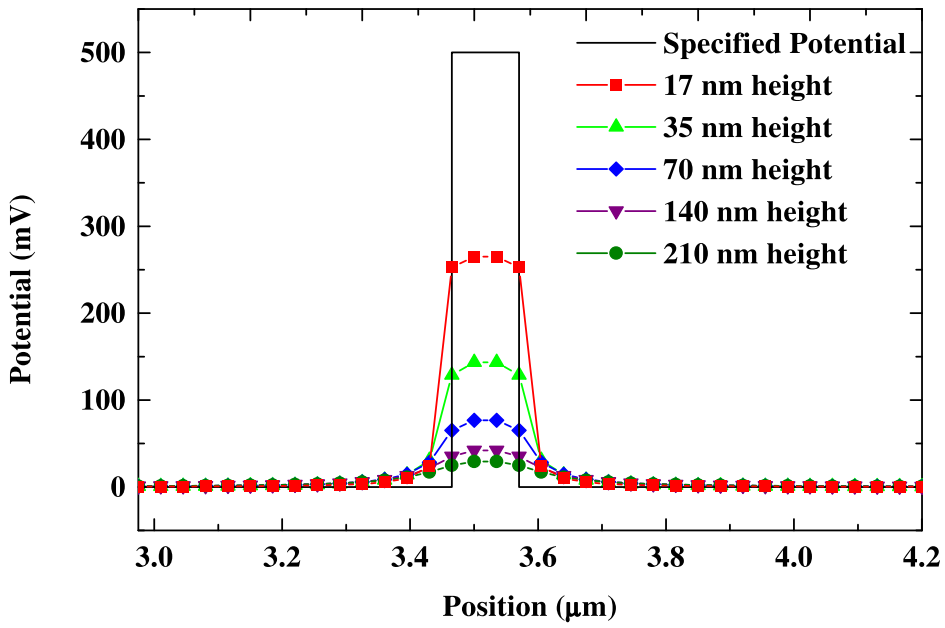

Fig. 3.11. Voltage vs. position profiles taken over a 150 nm $0.5V$ potential "dot". The cantilever used has a 18° half angle. The tip-sample distance was varied from 17 nm to 210 nm.

role in the KFM measurements. A wide tip will sample the surface potential over a larger area than a sharp tip. Surprisingly, this does not significantly decrease the spatial resolution of the electrostatic potential measurement, as seen in Figure 3.13. However, it does affect the value of the electrostatic potential measured by the KFM.

As seen in all the simulations, the electrostatic potential measured by the KFM is distorted by the long range electrostatic forces acting on a finite sized cantilever. The limiting factor in the spatial resolution and the accuracy of the electrostatic potential measurement is the finite–sized probe. The capacitive coupling between the beam and the surface is much smaller than the capacitive coupling between the tip and the surface, however the area of the cantilever beam is much bigger. As seen in the simulations, the effects of the small capacitive couplings integrated over the large area of the capacitor beam play a large role in the electrostatic potential measured by the KFM.

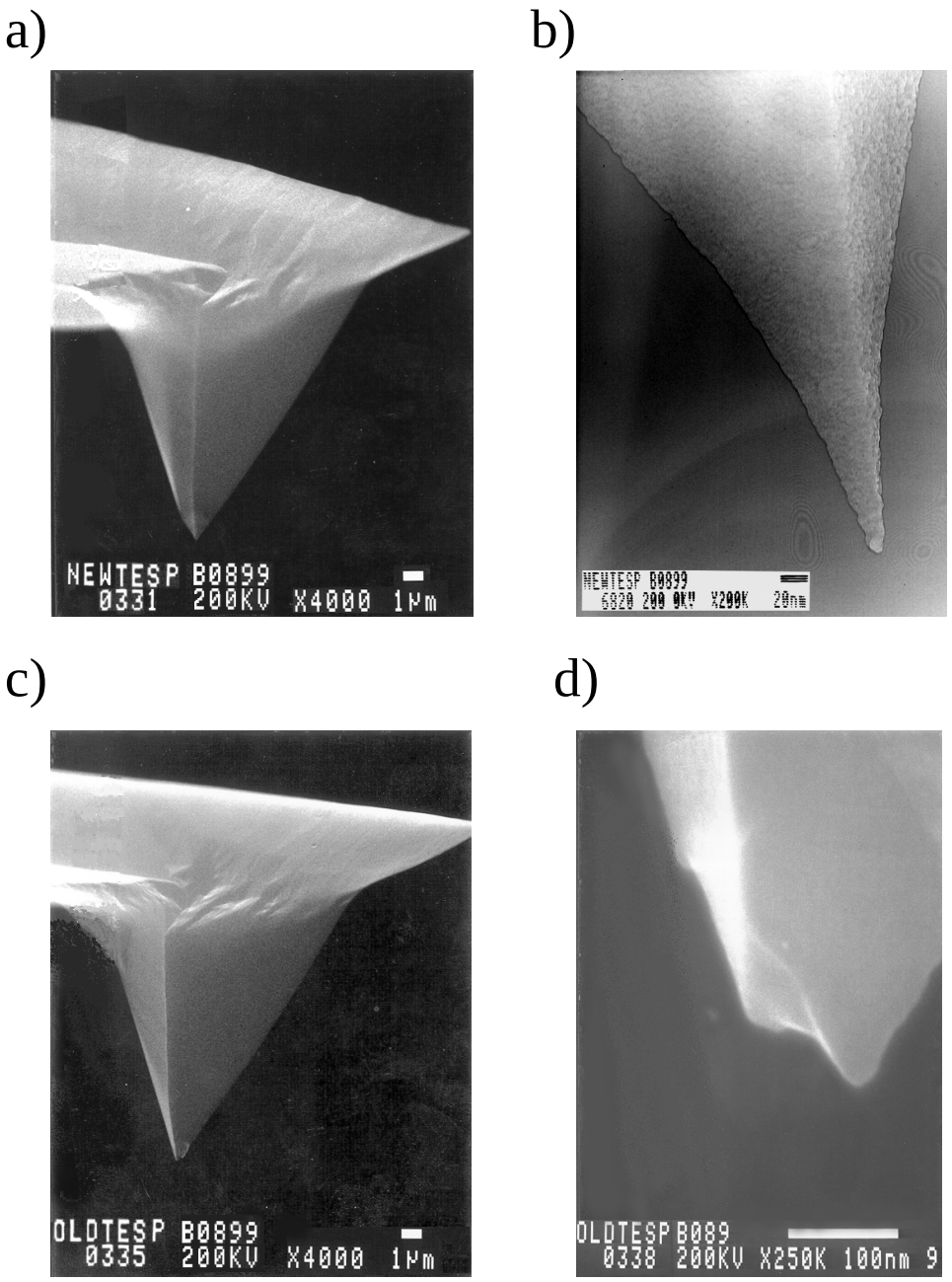

Fig. 3.12. a) SEM and, b) TEM images of a new cantilever. The measured end radius is ~ 3 nm. c), d) SEM images of a used AFM cantilever showing significant damage from use.

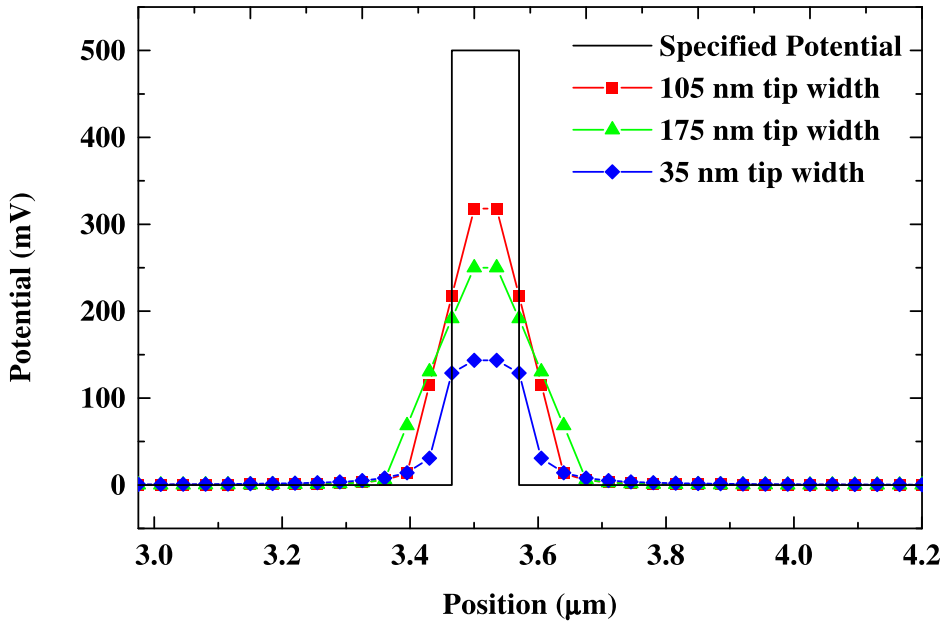

Fig. 3.13. The effects of blunting of the tip from use is modeled. Voltage vs. position profiles taken over a 150 nm wide 500 mV potential "dot". The cantilever used has a 18° half angle. The width of the cantilever tip was varied from 35 nm to 175 nm.

3.2 Simulations of KFM on Nanotubes

For both ballistic and diffusive transport, the electrostatic potential of the nanotube is known. Based on the knowledge of the electrostatic potential of the MWNT, and the geometry of the contacts, it is possible to solve Laplace's equation for the ideal electrostatic potential, and then apply the KFM convolution model developed earlier in this chapter.

3.2.1 Electrostatic model

A simple program has been developed to solve Laplace's equation in free space using a mesh relaxation approach. The resulting two dimensional map of $\phi(x, y)$ is useful in interpreting the electrostatic potential images from the KFM. The program solves Laplace's equation by iterating over a matrix that contains specified voltages on arbitrary conductors. (See Figure 3.14(a)) The algorithm is as follows: i) A matrix is defined and the boundary conditions are specified, ii) the new value for

each point in the matrix is calculated as the average of its four neighbors as:

$$\phi_{i,j}^{n+1} = \frac{1}{4}(\phi_{i,j+1}^{n} + \phi_{i,j-1}^{n} + \phi_{i+1,j}^{n} + \phi_{i-1,j}^{n}), \tag{3.15}$$

where n specifies the iteration number, iii) the boundary conditions are reapplied, and the procedure is repeated. The program terminates when the largest change in the potential from one iteration to the next is less than a specified tolerance.

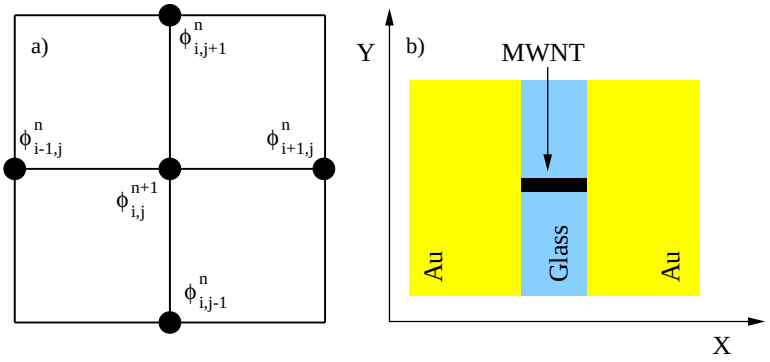

Fig. 3.14. a) Schematic of the relaxation method of solving Laplace's equation. The potential of the center element is the average of the four surrounding elements. b) Schematic of sample structure used in the simulations.

All simulations presented in this paper are spatially two dimensional (XY). A similar program was written to calculate the electrostatic potential in three dimensional (XYZ). For the given sample geometry, and the conditions specified for the KFM convolution simulations, the difference between the two dimensional and three dimensional solutions was negligible. The two dimensional version of the program was used due to time constraints. In all simulations the boundary conditions were designated to match the sample configuration of a 100 nm wide nanotube connecting two Ti/Au contact pads separated by 4.2μm as shown in Figure 3.14 (b).

3.2.2 Simulation of broken MWNT rope

A broken MWNT sample was simulated to study the effects of the convolution of the electrostatic potential present in the KFM method. *A priori* one expects each part of the broken MWNT rope to be held at a constant electrostatic potential, with the

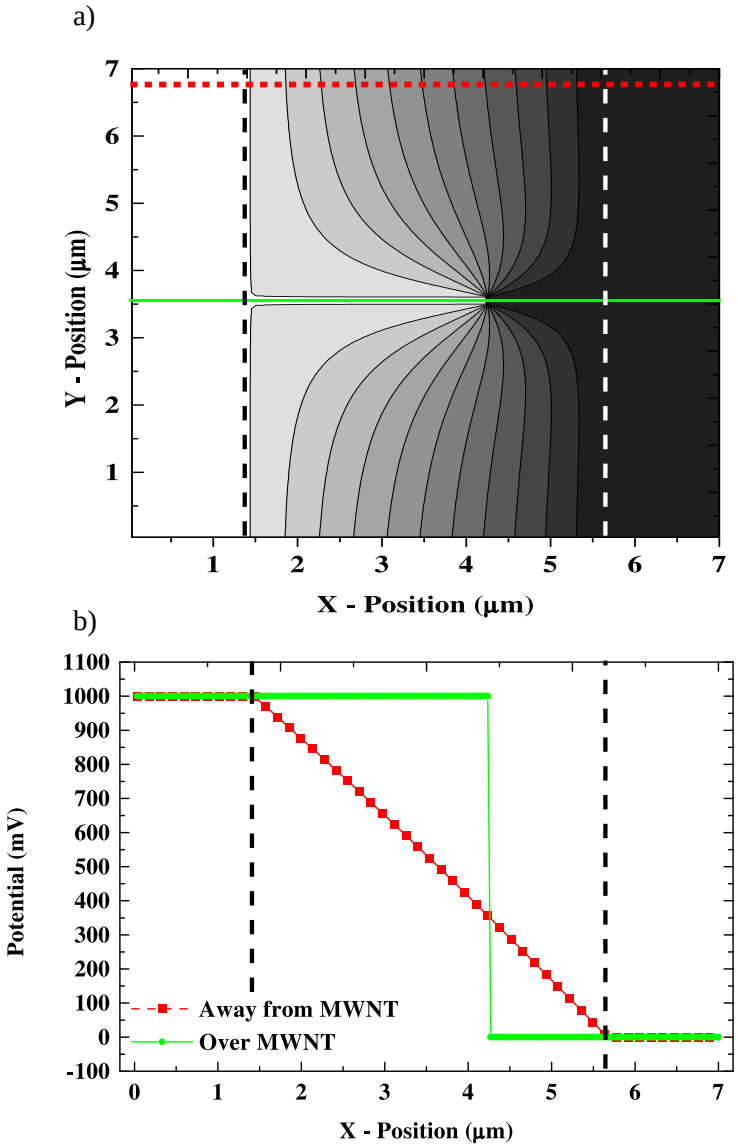

Fig. 3.15. a) An equipotential contour plot of the solution to Laplace's equation for a 100 nm diameter broken MWNT rope located at 3.5 μm along the Y–axis. The vertical dashed lines indicate the edge of the contacts. The contours are spaced at 91 mV/contour. b) Electrostatic potential vs. position sections taken away from the MWNT rope (squares), and over the MWNT rope (solid line).

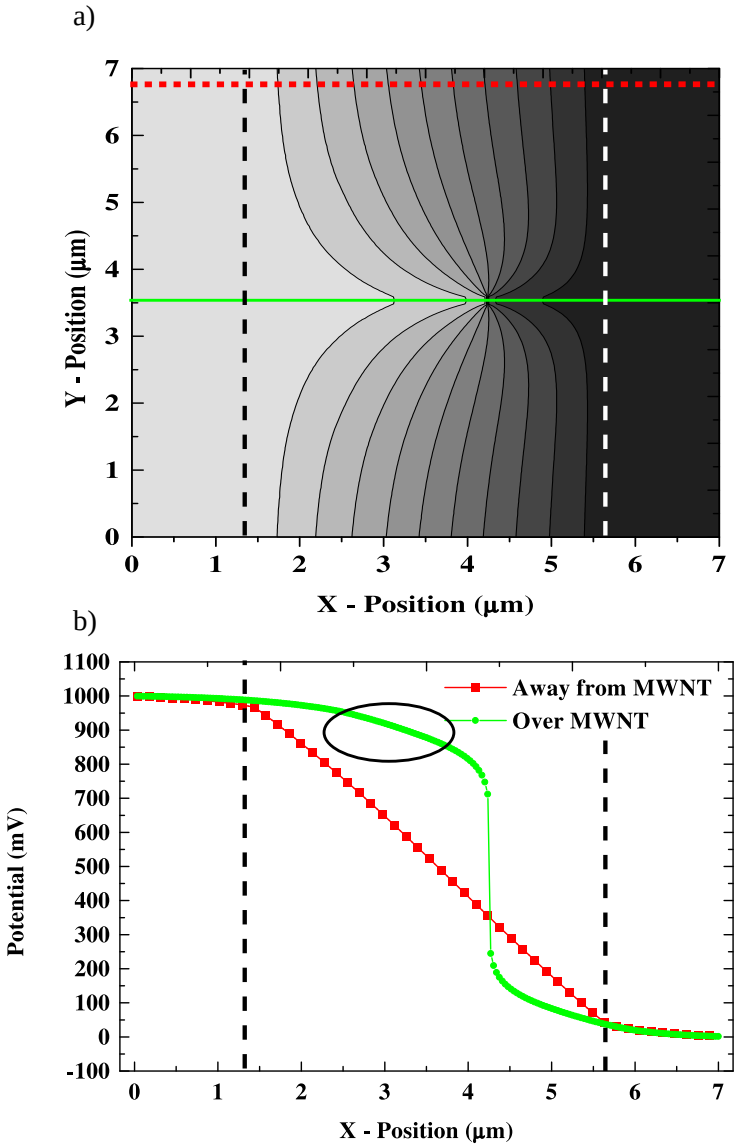

Fig. 3.16. The results from a simulation of a broken MWNT including KFM convolution effects. a) An equipotential contour plot for a 100 nm diameter broken MWNT rope located at 3.5 μm along the Y–axis. The vertical dashed markers indicate the edges of the contacts. The contours are spaced at 91 mV/contour. b) Electrostatic potential vs. position sections taken away from the MWNT rope (squares), and over the MWNT rope (solid line).

value depending on which contact the MWNT rope is contacting. The simulation was set up to model a 100 nm diameter MWNT rope spanning two contact pads separated by 4.2 μm. An equipotential contour plot of the solution to Laplace's equation for the electrostatic potential is shown in Figure 3.15. Markers indicate where potential cross-sections are taken. Far away from the nanotube, a linear decrease in the electrostatic potential is observed from one contact to the other. A cross-section taken over the top of the MWNT shows the discontinuity in the potential at the break in the MWNT.

The solution of Laplace's equation is then modified by taking into account the finite size of the KFM probe as described in the previous section. The AFM cantilever was modeled as having an 18° half angle and was held $\sim$ 17 nm above the surface. This model is a reasonable approximation of the geometry of the AFM cantilevers used to obtain the electrostatic potential data shown in the next chapter. The largest discrepancy between the model and the AFM tips is the size of the beam used. As seen in Figure 3.3 the beam extends $\sim 10\mu$m away from the tip. The reduction in the size of the beam was necessary due to constraints of the program. The results are shown in Figure 3.16. As shown, the potential profile over the MWNT shows a significant change. A slope of 59 mV/μm in the electrostatic potential vs. position profile over the simulated MWNT rope as indicated by the dark oval in Figure 3.16(c) was measured. This slope is due to the AFM tip measuring the electrostatic potential over the MWNT rope as well as the electrostatic potential on either side of the MWNT rope.

3.2.3 Simulation of a ballistic MWNT

Given the convolution effects of the KFM, what will the electrostatic potential vs. position profile look like for an ideal ballistic conductor? The sample was modeled as a $\sim$ 100 nm wide MWNT rope placed between two contacts separated by 4.2 μm. If we assume that the electrostatic potential is dropped symmetrically in each contact, we would expect a electrostatic potential profile as shown in Figure 3.17.

Again using the previously developed convolution program, the effects of the electrostatic potential convolution present in the KFM measurement technique can been

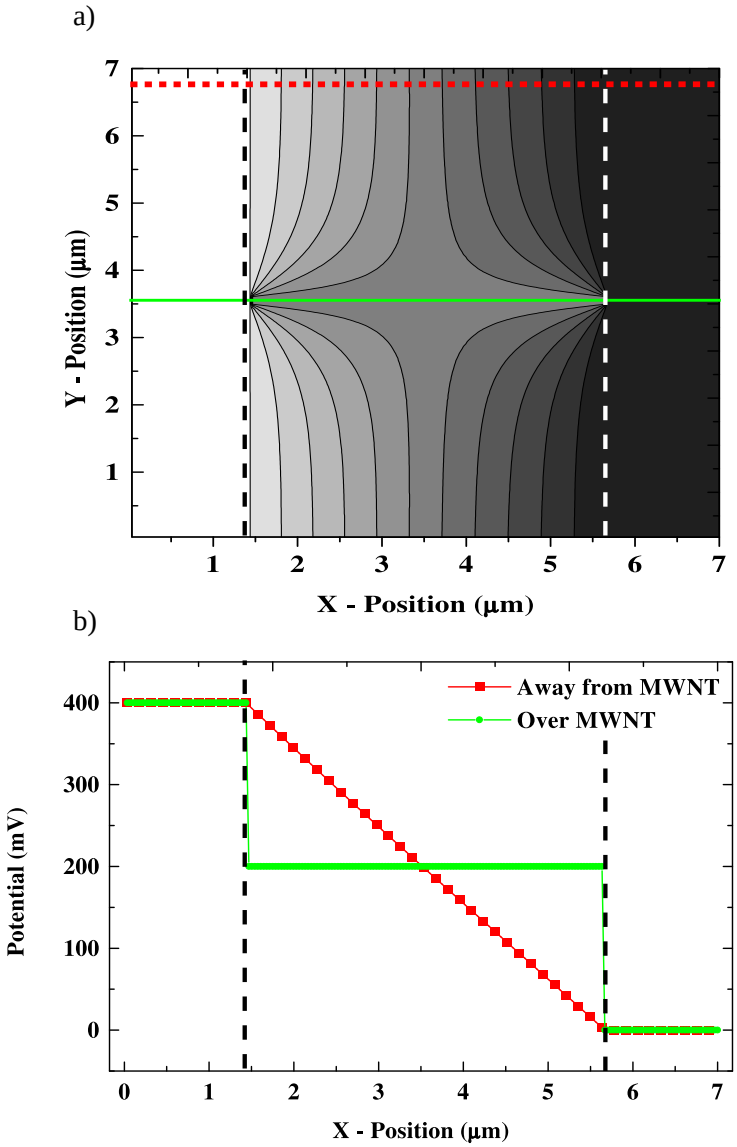

Fig. 3.17. The solution to Laplace's of a ballistic MWNT, located at 3.5 μm along the Y–axis, where all the electrostatic potential drop is in the contacts. a) An equipotential contour plot of the electrostatic potential, with vertical dashed lines indicating the edges of the contacts. The spacing between contours is 36 mV/contour. b) The electrostatic potential vs. position profiles over the simulated MWNT rope (solid line) and away from the MWNT rope (squares).

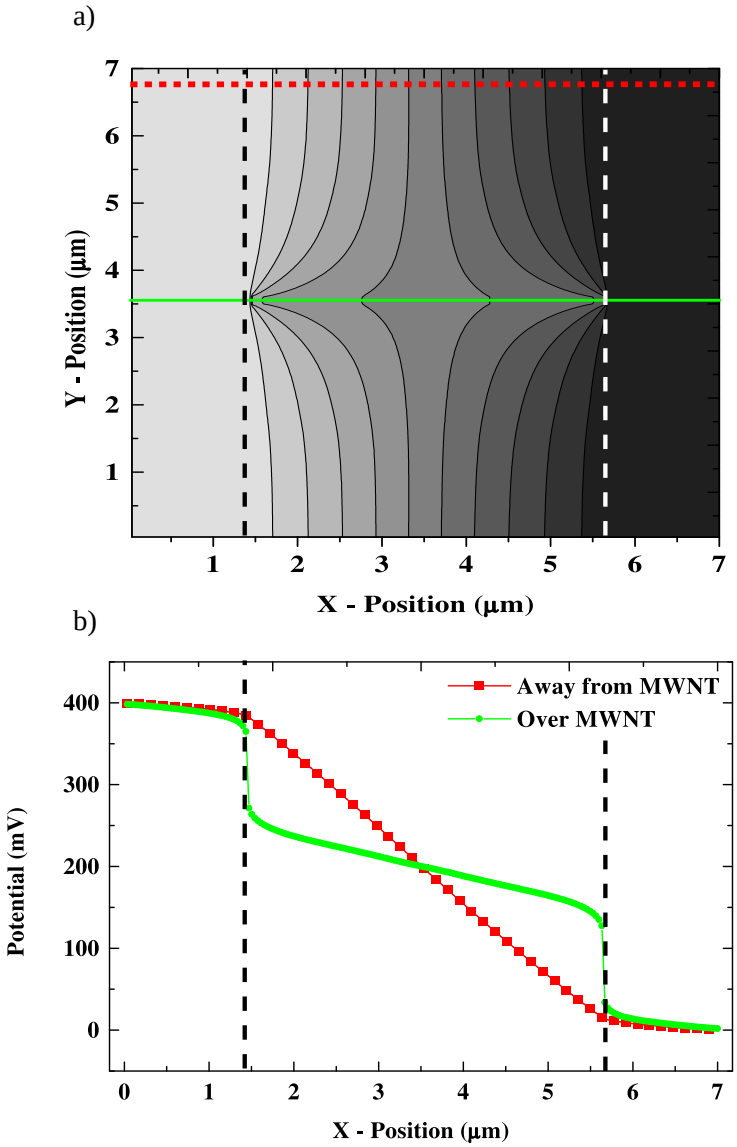

Fig. 3.18. Results from a simulation of a ballistic 100 nm diameter MWNT, located at 3.5 μm along the Y–axis, including KFM convolution effects. a) An equipotential contour plot of the electrostatic potential, with vertical dashed lines indicating the edges of the contacts. The spacing between contours is 36 mV/contour. b) The electrostatic potential vs. position profiles over the simulated MWNT rope (solid line), and away from the MWNT rope (squares).

seen. This simulation used a tip described by a half–angle of 18°, and a height above the sample of $\sim$ 17nm. The results are shown in Figure 3.18. As can be seen in the electrostatic vs. potential profile over the MWNT, there is a significant slope to the profile. The slope is 23 mV/μm which is about 25% of the slope away from the MWNT.

Solely from the electrostatic convolution effects present in the KFM, the stair case behavior of the electrostatic potential for an ideal ballistic MWNT will be modified. As seen in the simulation this, convolution is a non-negligible effect and needs to be accounted for when interpreting the data.

3.2.4 Simulation of a diffusive MWNT

A diffusive MWNT with small contact resistances ($\sim$ 25% of the overall resistance) was also simulated. The solution of Laplace's equation for a diffusive conductor is given in Figure 3.19. As in the ballistic case, the discontinuities in the electrostatic potential profile near located where the MWNT meets the contact are indicative of contact resistance. Figure 3.20 presents the results of modeling the electrostatic convolution present in the KFM method. As seen in Figures 3.19, and 3.20(c) the change in the electrostatic potential measured over the MWNT is small as compared to the results of the convolution of the ballistic MWNT. This exposes a characteristic of this convolution model, relatively small changes in the electrostatic potential will not be greatly affected by the convolution.

3.3 Summary

Presented in this chapter is the theory for the measurement of the electrostatic potential using the Kelvin force microscope. Ideally, this instrument will measure the local surface potential with the sensitivity to electrostatic potential of the Kelvin method, and the resolution of the AFM. However, due to the finite size and complicated geometry of the AFM tip/beam, the electrostatic potential recorded by the KFM is a weighted sum of all the surface potentials with the weighting factor being the derivative of the capacitance with respect to the tip/sample separation distance. As shown by a model developed to calculate the weighted sum, the spatial resolu-

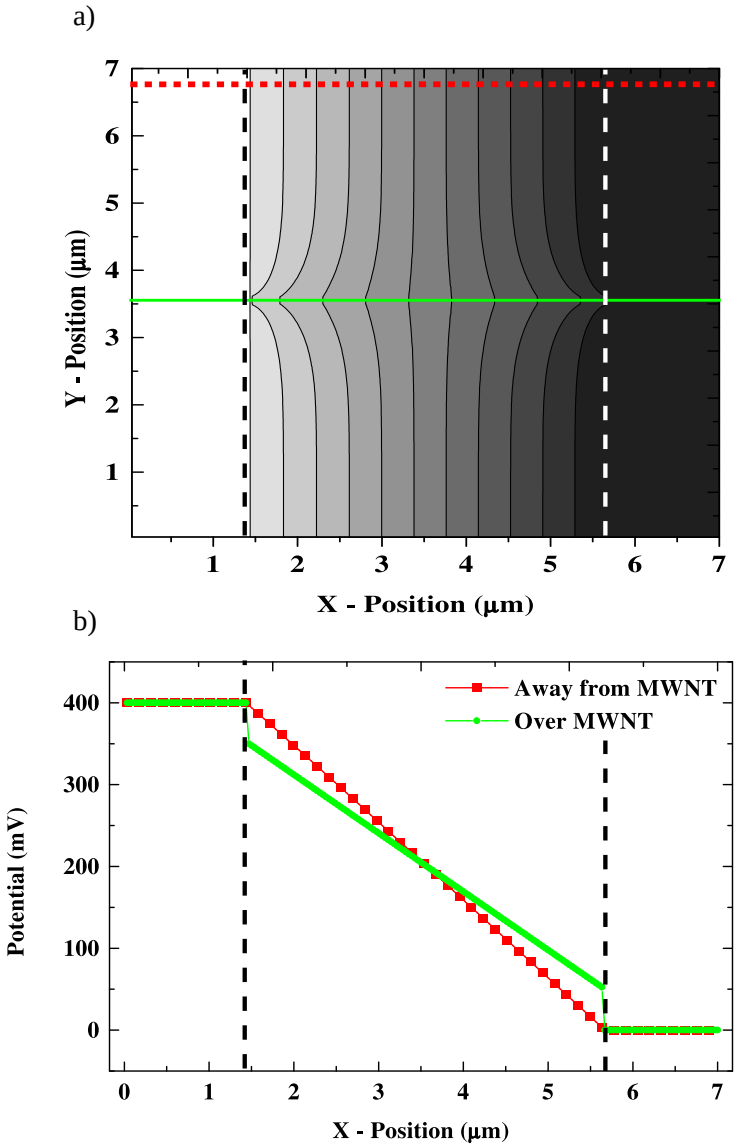

Fig. 3.19. The solution to Laplace's equation for a diffusive MWNT, located at 3.5 μm along the Y–axis, with a contact resistance of $\sim 25\%$ of the overall system resistance. a) An equipotential contour plot of the electrostatic potential, with vertical dashed lines indicating the edges of the contacts. The spacing between contours is 36 mV/contour. b) The electrostatic potential vs. position profiles over the simulated MWNT rope (solid line) and away from the MWNT rope (squares).

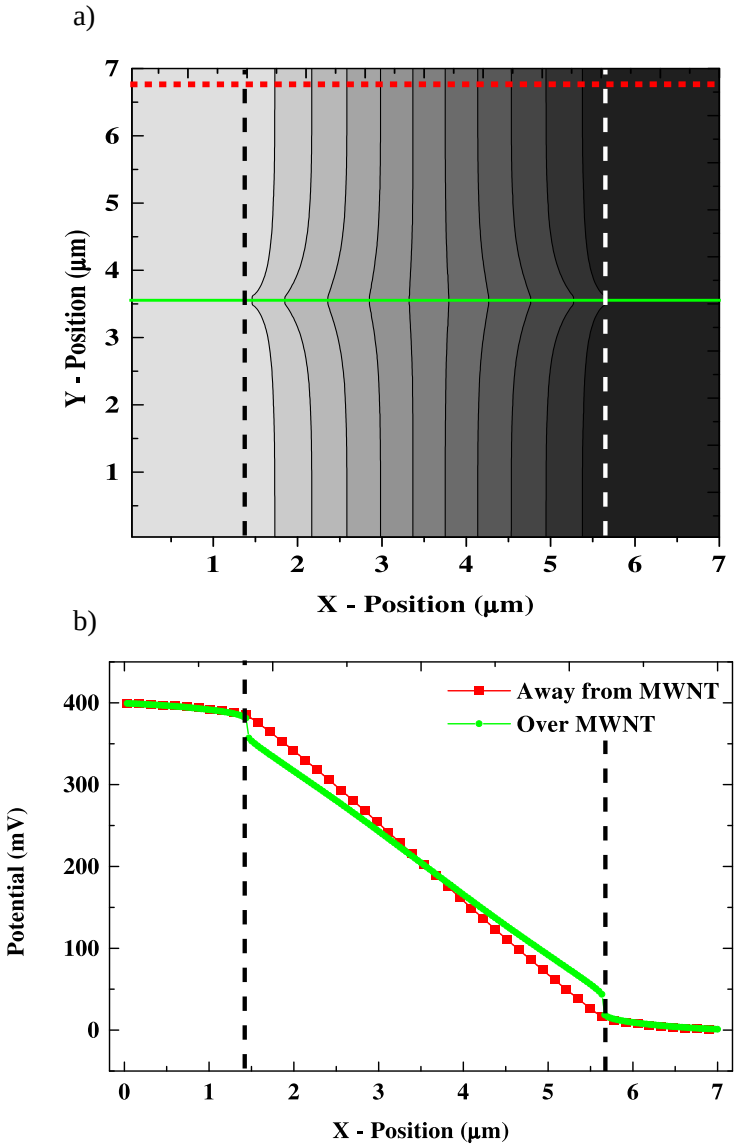

Fig. 3.20. Simulation including KFM tip effects on a 100 nm diameter diffusive MWNT, located at 3.5 μm along the Y–axis. a) An equipotential contour plot of the electrostatic potential, with vertical dashed lines indicating the edges of the contacts. The spacing between contours is 36 mV/contour. b) The electrostatic potential vs. position profiles over the simulated MWNT rope (solid line) and away from the MWNT rope (squares).

tion and the accuracy of the electrostatic potential is limited by the geometry of the tip/beam system.

Based on sample dimensions and the electrostatic potential profiles developed in Chapter two for the two transport mechanisms, a method has been developed to calculate a two dimensional map of the surface electrostatic potential. The application of the KFM convolution model to both a ballistic and a diffusive MWNT transport mechanisms indicates that if the contact resistance in the diffusive MWNT is small compared to the MWNT resistance, the KFM should be able to distinguish between the two transport mechanisms. However, in the case of the ballistic MWNT, a significant correction to the electrostatic potential vs. position profile must be considered.

4. KFM ON CARBON NANOTUBES

In order to gain insight into the transport properties of single ropes of multi-walled carbon nanotubes, the Kelvin force microscope has been used to measure the local electrostatic potential along a single rope of MWNTs that is ohmically contacted by Ti/Au pads. The sample fabrication procedure is based on a shadow mask technique. The technique allows low resistance contacts to be non-invasively placed on the ends of a single MWNT rope. The Kelvin force microscopy measurements to date have shown three types of behavior i) non-conductive samples, ii) potential drops correlated with changes in the morphology of the MWNT rope, and iii) a linear potential drop down the length of the MWNT bundle. The broken MWNT is used to estimate the electrostatic potential convolution effects of the KFM which are then applied as a correction to the measured potential of the MWNT that shows a linear potential drop. This sample can be analyzed in terms of both diffusive and ballistic transport.

4.1 Sample Preparation

In order to facilitate the electrical and potential measurements, a simple shadow-mask fabrication technique has been developed. This technique is a combination of a procedure developed by Michael Buss of Prof. Ronald Andres's group that he used to mount SWNTs and MWNTs onto atomic force microscope cantilevers,[50] and a procedure developed by Pedro de Pablo for fabricating 100 nm diameter gold wires. A schematic of this procedure is presented in Figure 4.1. An advantage to this method is the non-invasiveness of the technique. The MWNT are not exposed to any chemical processing that is present in other contacting technologies.[13] This minimizes the possibilities for unintentional doping or the formation of defects in the MWNT. Details of the sample mounts and positioners can be found in Buss's thesis. [50]

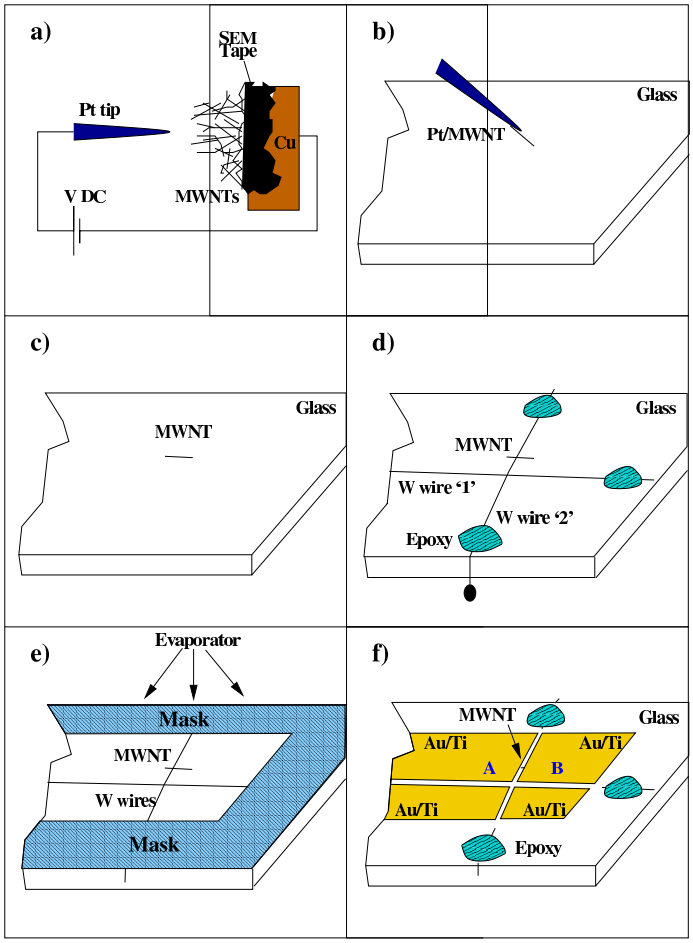

Fig. 4.1. A schematic diagram of the MWNT preparation procedure showing a) the selection and removal of a MWNT from the carbon felt, b) a MWNT adhering to the etched Pt tip, c) the transfer of the MWNT to the glass slide d) the placement of a micron diameter tungsten wire (wire '1'), roughly parallel to the MWNT, serves as a vertical riser to prevent contact between a second W wire, the shadow mask (wire '2'), which is oriented perpendicular to the MWNT, e) e-beam evaporation of a thin film (5 nm Ti followed by 150 nm Au) on to the ends of the MWNT, and f) the final MWNT after removal of the tungsten wire. After electrical contact is made to contact pads A and B, a robust sample results with both ends of the MWNT buried by the deposited Ti/Au film. [2]

Individual MWNTs or ropes of MWNTs are manipulated in the following manner. Etched platinum field emission tips (end radius of $\sim$ 100 nm) are fabricated using standard etching techniques. No. 2 glass cover slips are cut into 9 x 9 mm squares using a diamond scribe. A sample mount has been built that attaches to a micro-positioner mounted on the stage of an inverted darkfield microscope having an overall magnification of 750X. The sample holder is centered over the objective lens of the microscope. The cut glass cover slip is placed onto the mount and the top surface of the slide is brought into focus. The cut cover slip is then wiped with an optical cloth until the bulk of the particles on the surface are removed. It is advantageous to leave a small number of particles on the surface of the cover slip in order to aid in focusing on the correct surface. The cover slip and holder are then placed in a covered box to minimize further particulate contamination.

The next step involves selecting a single MWNT from the source. The nanotube source consists of a small copper sheet with one edge wrapped with conductive SEM tape, onto which the nanotubes (MWNTs or SWNTs) have been deposited in 3 or 4 places. The nanotube tape and a Pt tip are mounted on to opposing micro-positioners, on the stage of the inverted dark-field microscope. The minimum diameter nanotube which one can "see" with this microscope is $\sim$ 75 nm. The Pt tip and desired MWNT are brought into proximity. The end of the MWNT sticking out from the boule is opened by touching it with the Pt tip held at 15 V with respect to the boule. After reducing the potential on the tip to 0 V, a length of the protruding tube is brought into contact with the tip. After contact, a bias of about 5 V is applied and, as the Pt tip is withdrawn from the MWNT source, we find that a 5-10 μm long rope of MWNTs becomes attached to the tip and eventually breaks free from the source. TEM studies show that both ends of the MWNT rope are opened during this procedure [3]. The end of the MWNT that first makes contact with the Pt tip is opened by the initial touch of the biased Pt tip. The second end of the MWNT is opened when the selected tube (or rope) is separated from the MWNT source. In both cases a visible emission of light is often observed during this selection and separation procedure, implying the

presence of a localized, intense electrical arc. There is a strong correlation between the relative humidity in the sample preparation room and the ease of selecting a single MWNT. During periods of high humidity (60%), selecting a nanotube becomes much easier. The water layer present on the Pt tip may promote adhesion of the nanotube.

The nanotube source is removed from the micro-positioner and the mount holding the glass cover slip is reinserted into the positioner. The glass is approximately centered over the scope objective and the tip/nanotube is oriented so that the nanotube is closer to the glass than any other part of the Pt tip. Care must be taken to focus the microscope on the correct side of the cover glass. Because the cover slip is transparent, three surfaces will be seen in focus: i) the bottom of the cover slip, ii) the top of the cover slip, and iii) the reflection of the bottom surface from the top surface. The residual particles left on the top surface aid in focusing on the top surface of the cover slip.

The nanotube can be positioned with better than 50 μm lateral resolution on the surface. The nanotube is lowered until its end touches the glass surface. Then the tip is lowered more while moving away from the touching end of the nanotube. The nanotube will stay attached to the tip, sliding along the surface, until enough of its length is in contact with the cover glass so that it sticks and the tip slides away (Fig. 4.1(c)). The Pt tip is then removed.

Two tungsten wires are placed on the glass. The first "support" wire is positioned parallel to the nanotube $\sim 10\mu$m away. The wire is stretched across the center of the substrate and held under tension (Fig. 4.1(d), wire '1'). This is done by attaching a weight ($\simeq$ 5 mm diameter solder ball) to one end of the wire and placing the other in a micro-positioner. Once in place the tungsten wire is glued (using Devcon 5 minute epoxy) to the edges of the cover glass. When dry the weight is cut free and the wire is cut loose from the sample mount.

The sample is carefully rotated 90° and the nanotube is relocated. Following a similar procedure, the second "shadow" wire is carefully placed perpendicular to the nanotube such that the ends of the nanotube are visible from either side of the wire

(as seen in Figure 4.1(d), wire '2'). Extreme care must be taken while putting glue drops onto the sample; the shadow wire is easily moved. The epoxy is allowed to dry for 30 minutes, and then the sample is carefully placed in a vacuum desiccator. Each sample requires ~ 5 hours preparation time.

After several samples have been made, they are inserted into a multi-source electron beam evaporator. A holder has been designed to mask the drops of epoxy present on the glass to prevent their coverage by the evaporated metal. We typically evaporate a $\sim$5 nm thick Ti adhesion layer followed by $\sim$150 nm of Au. Once the contact pads have been deposited, the sample is inspected in the darkfield microscope, the wires are removed, and the sample can be imaged with an atomic force microscope (AFM). From the resulting images, it is usually clear which samples have survived the handling while transferring the samples into and out of the evaporation chamber. A representative image is given in Figure 4.2 and shows a detail of one end of the MWNT that is under the evaporated Ti/Au film.

We find that the electrical contacts made with this method require precautions during handling. The samples are very prone to destruction by static discharge. The use of a grounding strap while handling the samples is recommended. The glass substrate is also very delicate, and flexible. A number of MWNT samples have failed at the edge of the Ti/Au contact possibly indicating that flexing of the substrate is pulling the MWNT ropes apart. If suitable precautions are used, these samples can be manipulated with ease. Early measurements of a sample's resistance were taken with a hand-held multimeter.

AFM images of two samples are illustrated in Fig. 4.3 (a) and (b). [3] In Figure 4.3 (a) we show a AFM image of an electrically continuous sample with two evaporated Ti/Au contact pads covering the ends of a MWNT. A common failure mode for the nanotubes appears to be an electrostatic discharge which evidently causes a high current to pass through the nanotube. An example of this failure mode is illustrated in Fig. 4.3 (b) which shows a nanotube that has been completely destroyed. The Ti/Au contacts appeared to be peeled back from the glass. Although the cause of this

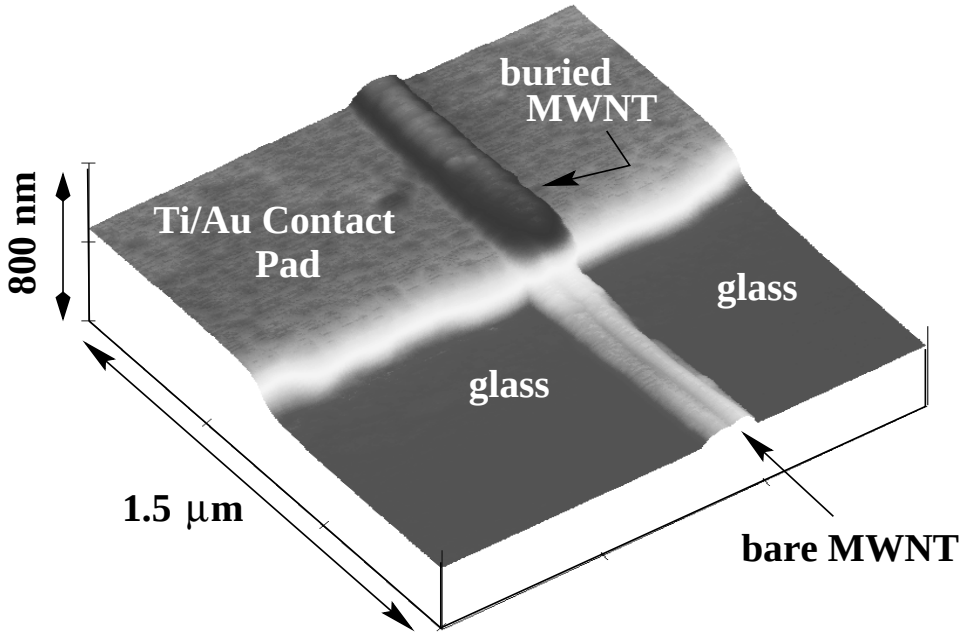

Fig. 4.2. A 1.5 μm x 1.5 μm AFM image of a MWNT rope buried under a Ti/Au contact pad. The image shows the substrate comprised of a glass cover slide, one of the two Ti/Au contact pads, a section of the MWNT buried under the Ti/Au film and a section of the bare MWNT which emerges from under the Ti/Au contact pad. [2]

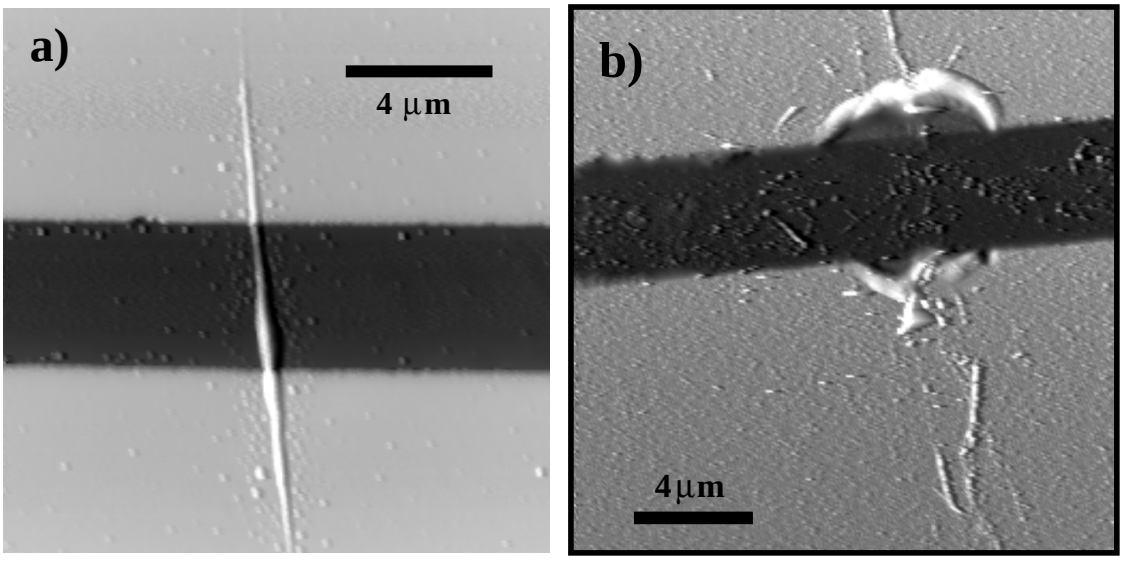

Fig. 4.3. a) An AFM image of a typical MWNT sample. The image shows a MWNT crossing a 4.3 μm wide trench. The two evaporated Ti/Au contact pads lie on top of the ends of the nanotube. b) An AFM image of MWNT sample that has been blown apart, presumably by an electrostatic discharge. Remnants of the MWNT are found scattered throughout the image. [3]

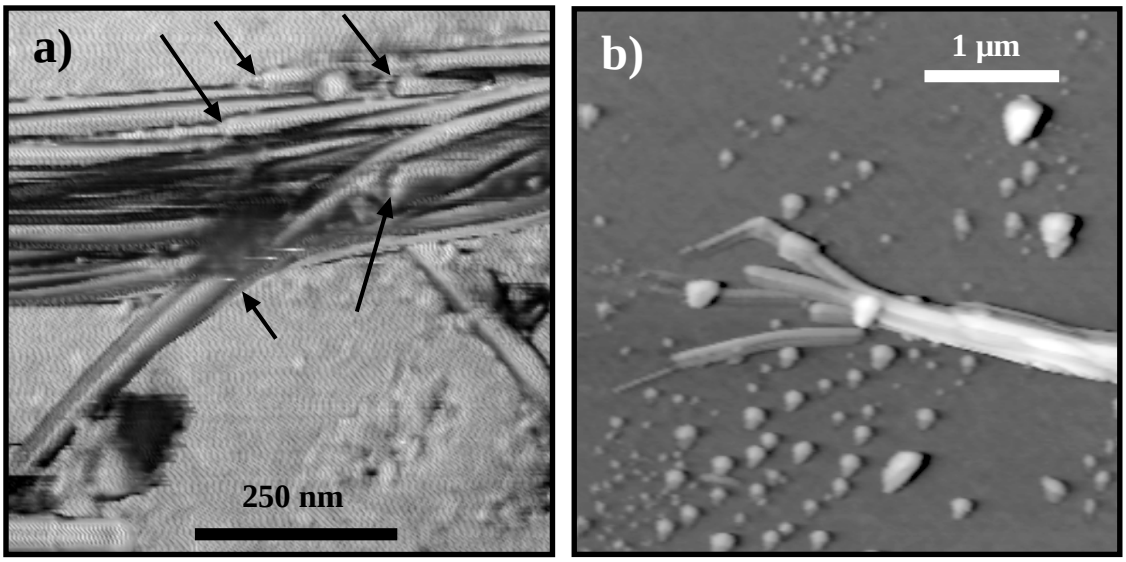

Fig. 4.4. a) An AFM phase contrast image of sample showing multiple nanotubes in a MWNT rope. This image was taken near the middle of the MWNT sample and reveals the ends of several MWNTs (see arrows), suggesting that only a few MWNTs remain electrically continuous across the entire 4.3 μm distance between the two contact pads. b)An AFM image of sample showing the individual MWNTs unraveling at the end of the rope. The diameters of the individual MWNTs in both images are enlarged due to tip dilation effects. [3]

damage is unknown, it may be indicative of localized heating prior to the destruction of the nanotube.

TEM studies suggest that a typical MWNT sample is comprised of a few individual MWNTs. [3] Further evidence supporting this view is given in Figures 4.4 (a) and (b) which illustrate how individual MWNTs intertwine in our samples. Figure 4.4 (a) is a phase contrast AFM image taken near the center of a mounted MWNT. The phase imaging mode is used to enhance contrast.[51, 52, 53] This image provides clear evidence that broken MWNTs exist along the length of the rope. Figure 4.4 (b) shows individual MWNTs that have unraveled at the end of a MWNT rope. Based on these studies, it is likely that few, perhaps only one, of the individual MWNTs in a rope remain continuous across the entire 4.3 μm length between the contact pads. Thus experimental transport measurements in our samples may be dominated by the electronic properties of only one MWNT.

4.2 Instrumental Considerations

The AFM used in this study was a Digital Instruments Nanoscope IIIa with a Multi–Mode AFM head. All electrostatic potential data were acquired using the "tapping/lift" mode of the instrument. This mode is a two-pass technique which measures the topography and the electrostatic potential in sequential passes across each scan line. During the first pass over a given scan line, the topography is measured using tapping mode AFM. A second pass over that same scan line is then immediately performed while maintaining a constant user specified height above the surface. Because the tip-sample separation is constant, the forces measured during the second pass will be free of the effects of the Van der Walls interactions. As seen in Chapter 3 maintaining a constant height above the surface is critical for minimizing the electrostatic potential convolution effects of the KFM. The topography and electrostatic potential images consist of a 256 x 256 bitmap of 16 bit values. In general the data is acquired at 0.25 to 0.5 Hz per scan line, yielding an acquisition time of 17 to 8.5 minutes per image respectively. For all data presented, the AFM tip was approximately 15 - 20 nm above the surface during the lift portion of the scan. This

distance was set by lowering the lift height until the tip would intermittently contact the surface, or the electrostatic potential feedback loop would become unstable.

Heavily doped uncoated tapping mode AFM cantilevers ($k \simeq 40-100$ N/m) were used for all data shown in this study. Uncoated cantilevers were chosen because they offer the sharpest tips, higher durability than metal coated tips, and some additional protection for the sample. Both gold coated, and cobalt chrome coated tips were tried, and both showed a slight reduction in the spatial resolution of both the topography and the electrostatic potential. Because of the high resistance of the cantilever, there is an issue of how fast the voltage applied to the tip can be modulated. Modeling the cantilever–sample system as a 20μm x 40μm parallel plate capacitor, the "RC" time constant can be calculated (C=0.44 fF , R $\simeq$ 2 MΩ). [47] This time constant is much smaller than any other characteristic time used in data acquisition. As seen in Chapter 3, the force on the AFM cantilever is proportional to the applied AC voltage. Best results for the electrostatic potential measurement were obtained when an AC voltage of 8 V was applied to a tip $\sim$ 15nm above the surface. The small separation between the tip and the surface resulted in the tip intermittently coming into contact with the surface while traversing a complicated topography (i. e. near the edges of the contacts). The high resistance of the uncoated cantilever does not allow appreciable current to flow if the tip contacts the surface. Because of the low resistance of metallic cantilevers, any contact results in a relatively large current flow, possibly damaging the sample and usually damaging the end of the tip.

The AFM is enclosed in an environmental control box. During these studies, when needed, dry nitrogen was pumped into the box to reduce the relative humidity. In all the data shown below, the relative humidity was less than 30%.

The KFM is sensitive to all electrostatic potentials including variations in the work functions of different materials and surface charge stored in the glass trench. A two pass technique was developed in order to remove the influences of these bias independent potentials. An electrostatic potential image is acquired as described above with no applied bias to the sample. Immediately following, a second pass is then

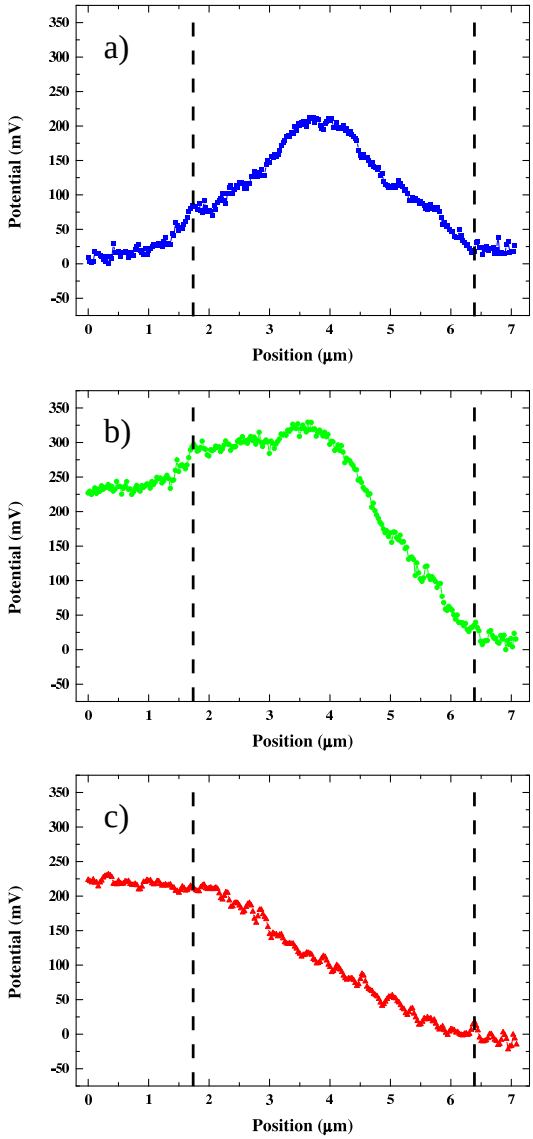

Fig. 4.5. a) The electrostatic profile from a MWNT sample far away from the MWNT rope at zero bias. The vertical dashed lines denote the edges of the trench. The electrostatic potential measured in the middle of the trench is dependent on the relative humidity, increasing as the relative humidity is lowered. b) An electrostatic potential profile taken over the same area with 0.4 V bias applied to the sample. c) The red curve is the difference between the green and the blue curves, the linear decrease in potential is expected from the solution to Laplace's equation.

taken with a bias applied to the sample. The two potential images are then subtracted. The resulting electrostatic potential image is from bias dependent potentials only. This is shown in Figure 4.5. Due to the slow scan rate and limited scan size the hysteresis present in the piezo scanner is minimized, for all the data shown the registration between two successive images was within 25 nm.

4.3 Broken MWNT Rope

Since the samples are rather delicate, there were many opportunities to study non-conductive (broken) MWNTs. Figure 4.6 shows data taken from a broken MWNT sample (Sample 1). Concentrating on the electrostatic potential vs. position profiles shown in 4.6 (c), there are two effects to note. The applied bias across the sample was 1 V, as is shown the measured electrostatic potential drop across the trench well away from the nanotube is 700 mV. This reduction in the measured potential is due to the effect of the cantilever beam sampling the electrostatic potential on each side of the trench. In all the data shown, the difference between the applied bias and the measured electrostatic potential drop across the trench was 20% – 30%. For this reason, only relative potential drops are measured. This is not a great limitation, since the overall system resistance is known, the relative values of the potentials can be converted into values for the resistance.

The second effect was demonstrated in the simulation of the broken MWNT in the last chapter. There is a significant slope to the electrostatic potential vs. position profile taken over the MWNT. In this case, the slope is ~ 50 mV/μm which is $\sim 20\%$ of the slope measured away from the MWNT. This is the effect of the AFM cantilever sampling the electrostatic potential away from the MWNT. It is expected that for smaller MWNT rope this slope will increase. For a similar sized MWNT the slope found on the broken MWNT can be used as a rough estimate for a correction to the slope of the measured electrostatic potential profiles. However, this correction is only valid if the imaging conditions and the samples are similar.

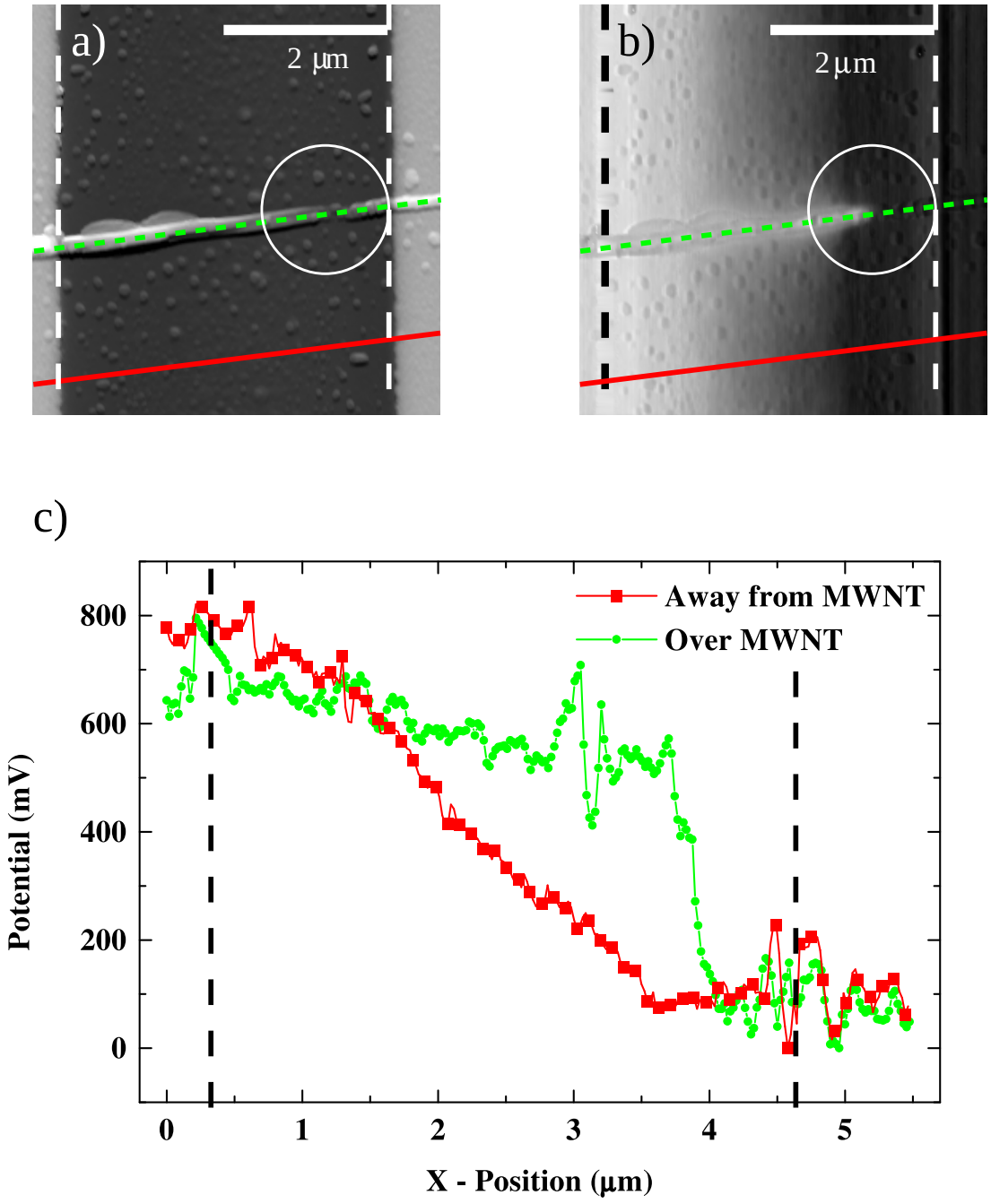

Fig. 4.6. a) The topographic image a broken MWNT sample, the measured height of the bundle is ~ 100 nm. b) The electrostatic potential image with vertical dashed lines indicating the edges of the contacts, and green dotted and red solid lines denoting where the electrostatic potential profiles were taken. c) The resulting electrostatic potential vs. position profiles.

4.4 MWNT with Structural Defects

The role of defects in nanotubes is of great interest. Several groups are using tube–tube junctions to probe the electronic structure of SWNTs. [54] Tube–tube junctions may also be used as a molecular switch, or rectifying diode. If one considered the use of carbon nanotubes for current carrying elements of future devices, defects in the structures may be failure points, due to high power dissipation at the defect. As seen in Figure 4.7, Sample 2 exhibits a sharp potential drop near a large structural change in the MWNT rope. During scanning, this nanotube abruptly changed resistance values from 15.2 kΩ to 32 kΩ; all the electrostatic potential data shown are after the resistance change. I(V) measurements indicate that this nanotube has linear I(V) characteristics up to ±400 mV. Profiles of the electrostatic potential taken down the length of the nanotube indicate that $\sim 40\%$ of the overall voltage drop is localized in an area of the MWNT rope where the rope appears to fray.

This MWNT does not display any potential drops at the contacts which may be indicative of diffusive transport, or ballistic transport with many available conduction modes. If transport is diffusive, the defect in the MWNT acts as a large resistance in series with the intrinsic MWNT resistance. Another possibility is that the transport is occurring through a MWNT located near the center of the rope. The broken MWNTs that surround the current carrying MWNT may tie the measured electrostatic potential to the potential of one of the contacts. The sharp electrostatic potential drop may be due to measuring the electrostatic potential from the broken MWNTs, not the current carrying MWNTs. With this method it is not possible to determine if this is the case.

4.5 MWNT Exhibiting Linear Potential Drop

Sample 3 exhibited a linear electrostatic potential drop down the length of the MWNT rope. During this study the MWNT rope had a resistance of ~ 12.8 kΩ. The topographic image of this sample is given in Figure 4.8 (a). Electrostatic potential profiles are taken down the length of the nanotube and far away from the MWNT as shown in Figure 4.8 (b). These profiles are shown in Figure 4.8 (c). This nanotube

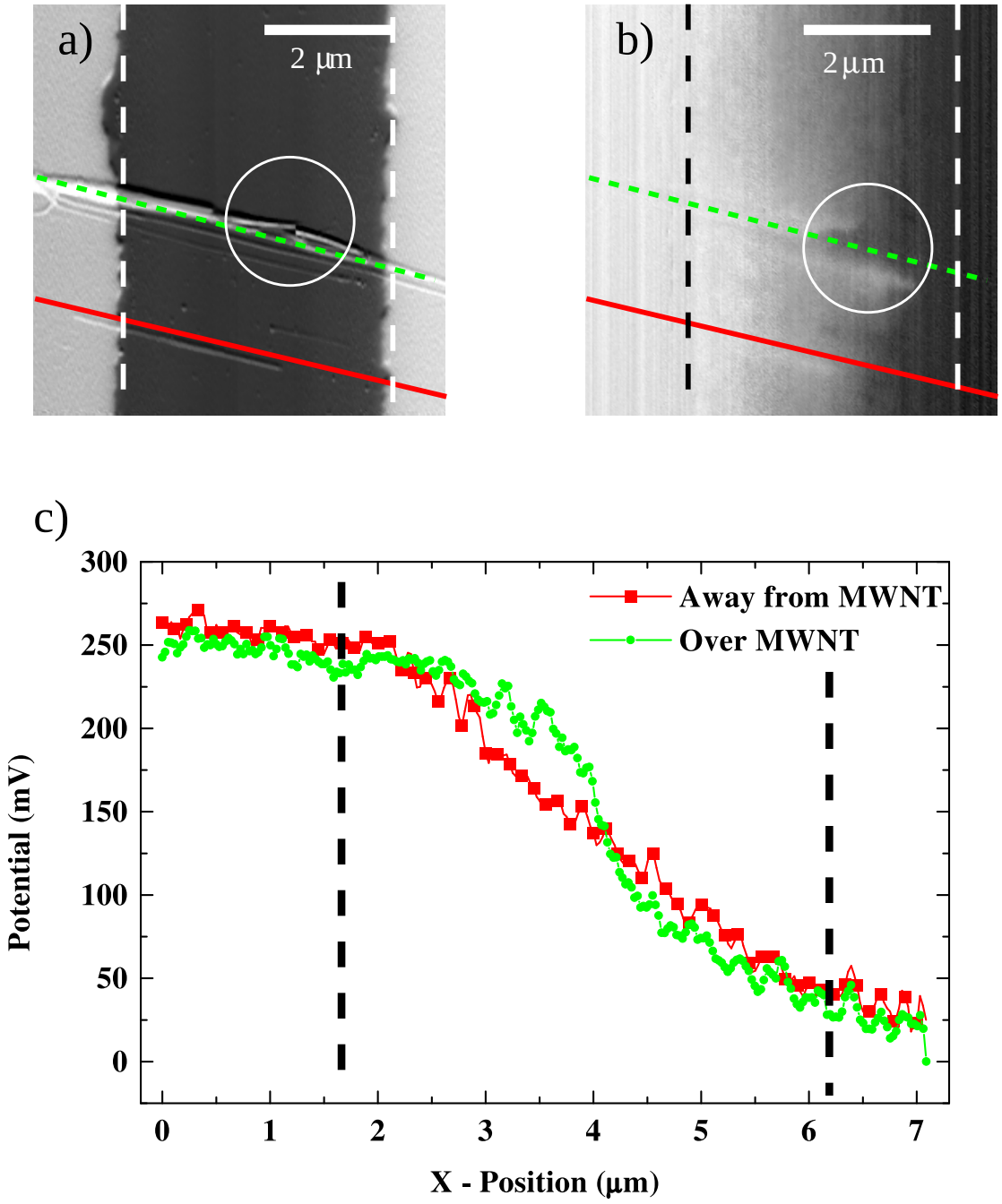

Fig. 4.7. a) The topographic image of a MWNT with a large structural change in the MWNT rope. b) The electrostatic potential image with vertical dashed lines indicating the edges of the contacts, and green dotted and red solid lines denoting where the electrostatic potential profiles were taken. c) The resulting electrostatic potential vs. position profiles.

shows a linear potential drop down the length of the nanotube and localized potential drops at each contact. The electrostatic potential data can be analyzed in terms of diffusive transport and ballistic transport if scattering centers within the MWNT are included.

The applied voltage is 420 mV, however the measured potential drop across the sample is 300 mV. As in the case of the broken MWNT, the cantilever beam extends over both sides of the trench reducing the measured electrostatic potential drop across the trench by about 25%. This effect complicates the interpretation of the electrostatic potential map. The effects of the reduction in the measured electrostatic potential drop can be minimized my measuring the electric field, given by the slope of the electrostatic potential vs. position profile, in the middle of the trench. This allows the use of the known applied bias, and the measured current through the MWNT rope to calculate resistance values.

The applied voltage is 420 mV and the width of the trench was measured to be 4.2 μm. The expected electric field in the trench is 100 mV/μm. Taking the slope of the electrostatic potential profile in the center of the trench 1 μm away from each contact, $\sim 3\mu$m away from the nanotube yields an electric field of 98 mV/μm. Performing a similar measurement over the MWNT yields an electric field of 60 mV/μm. Assuming the electric field along the MWNT is constant, multiplying the slope of the line fit to the electrostatic potential vs. position profile and distance between contacts (4.2 μm) yields a voltage drop of $\sim$ 250 mV. The remaining $\sim$ 170 mV is symmetrically dropped, $\sim$ 85 mV per contact. During these measurements, the MWNT was carrying 33.1 μA of current. From this analysis, the resistance of the nanotube is calculated to be $\sim$ 7.6 kΩ; each contact had a resistance of $\sim$ 2.6 kΩ. If slightly different profiles are taken over the MWNT, the value for the electric field measured over the MWNT varies by about 10%. Using this rough estimate for the uncertainty in the measurement of the electric field, all measured values are considered accurate to within 10%.

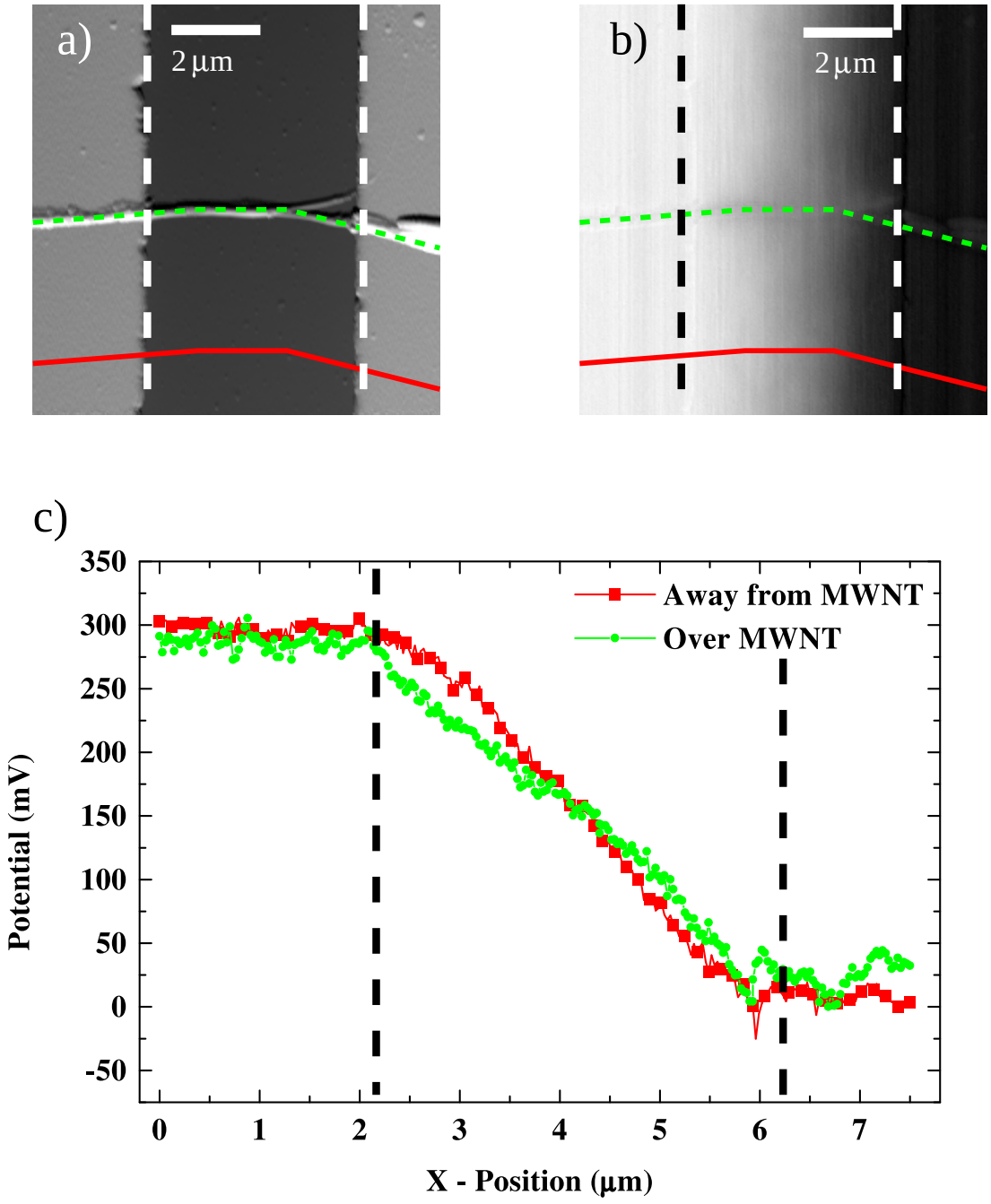

Fig. 4.8. a) The topographic image of a MWNT, the measured height of the bundle is $\sim$ 100 nm. b) The electrostatic potential image with vertical dashed lines indicating the edges of the contacts, and green dotted and red solid lines denoting where the electrostatic potential profiles were taken. c) The resulting electrostatic potential vs. position profiles.

The values calculated above do not account for any effects of the electrostatic potential convolution present in the KFM measurement technique. This MWNT rope was of similar size to that of the broken MWNT rope sample (Sample 1) analyzed in Section 4.3. The slope of the electrostatic potential vs. position profile measured over the broken section of the MWNT rope was about 20% of the slope measured away from the MWNT rope. Based on this information, the convolution effect in Sample 3 can be roughly corrected for by subtracting 20% from the electric field measured over the MWNT. Application of the correction results in a reduction of the MWNT resistance to $\sim$ 6.1 kΩ, and the increase in contact resistance to $\sim$ 3.4 kΩ per contact. The uncertainty in the resistance measurement introduced by this correction is unknown, it is highly dependent on how well the geometry of the broken sample matches with this sample. The 20% correction in the measured slope of the electrostatic potential vs. position profile is commensurate with the results of the simulations presented in Chapter 3.

Note, it is important that the electric field is measured away from the contacts. Within 1μm of each contact the potential measured on the nanotube is affected by the potential of the gold contact. Also, the MWNT rope in this sample did not lie in a straight line across the contacts.

Since an approximate value for the intrinsic MWNT resistance is now known, what can be said about the transport mechanism? If transport is diffusive we can extract an approximate value for the conductivity (σ) of this sample. Rewriting Equation 2.4 from Chapter 2 we have:

$$I = VG \quad \text{where} \quad G = \frac{\sigma A}{L}, \tag{4.1}$$

where A is the cross sectional area of the conductor, and L is the length of the sample. Solving for the conductivity σ yields

$$\sigma = \frac{GL}{A}. \tag{4.2}$$

In this case the cross sectional area of the conductor is ill–defined. As detailed

in Chapter 2, the number of MWNTs that comprise the rope, and the number of MWNTs that are continuous across the gap between contacts are unknown. In order to estimate the conductivity of the MWNT, it is assumed that the current density is uniform within the MWNT rope. Based on the sample dimensions the maximum possible diameter of the MWNT rope is 50 nm, which yields a conductivity of $\sigma = 1.1^{-7}$ Ω·cm. Conversely the minimum observed diameter of the MWNTs used in this sample is 5 nm, which yields a conductivity of $\sigma = 1.1^{-9}$ Ω·cm. These value for the conductivities are comparable to values of conductivity measured for graphite fibers. [55] However, if the current flow is through a single or a small number of the metallic shells that comprise the MWNT rope, the assumption of a uniform current density is not valid.

Even though the measured conductivities of this MWNT are similar to the conductivities of carbon fibers subject to diffusive transport, the ballistic transport model must still be considered. There is experimental [2, 20], and theoretical evidence for ballistic transport with mean free paths of greater than 10 microns. [38] Also, the temperature dependence of the transport properties of MWNT are different than that of carbon fibers. [24, 42, 55] From the electrostatic potential measurement, this sample does not show the behavior expected for an ideal ballistic MWNT as shown in Chapter 3.2.3. However, since this sample shows some contact resistance, it is possible to analyze it in terms of ballistic transport if the effects of defects or scatters in the MWNT are taken into account. The resistance of a nanotube with scatters can be written in two parts: i) contact resistance, and ii) MWNT resistance from scatters. The resistance of the entire system is given by: [4]

$$R_{total} = G_{total}^{-1} = \frac{h}{2e^2 MT}, \tag{4.3}$$

where M is the number of available conduction modes, and T is the transmission probability.

This system resistance R_{total} can be rewritten as:

$$\begin{aligned} G_{total}^{-1} &= \frac{h}{2e^2MT} \\ &= \frac{h}{2e^2M}(\frac{1}{T}-1)+\frac{h}{2e^2M} \\ &= \frac{h}{2e^2M}(\frac{1-T}{T})+\frac{h}{2e^2M} \\ &= G_{nt}^{-1}+G_{mm}^{-1}, \end{aligned}$$

where $G_{nt}^{-1} = \frac{h}{2e^2M}(\frac{1-T}{T})$ is the MWNT resistance, and $G_{mm}^{-1} = \frac{h}{2e^2M}$ is the total contact resistance from mode–matching. Based on the measured system and contact resistances, the number of conduction modes and the transmission probability can be estimated.

The total contact resistance of this sample was 6.8 ± 0.6 kΩ. The number of modes can be found by writing the expression for the mode–matching contact resistance as

$$M = \frac{h}{2e^2G_{mm}^{-1}} \tag{4.4}$$

$$\approx \frac{12.9\text{k}\Omega}{G_{mm}^{-1}} \approx 1.9 \pm 0.2 \tag{4.5}$$

The number of conduction modes must be an integer, and will be taken to be $M = 2$.

The number of modes and the MWNT resistance $G_{nt}^{-1} = 6.1 \pm 0.6$ kΩ can be used to calculate the transmission coefficient. The nanotube resistance G_{nt}^{-1} can be written as:

$$G_{nt}^{-1} = \frac{h}{2e^2(2)}(\frac{1-T}{T}) \tag{4.6}$$

This expression can be solved for the transmission probability T

$$T = [\frac{G_{nt}^{-1}}{12.9\text{k}\Omega}+1]^{-1} \tag{4.7}$$

Inserting $G_{nt}^{-1} = 6.1 \pm 0.6$ kΩ into Equation 4.7 the transmission probability is $T = 0.67 \pm 0.06$ From this result, 2/3 of the electrons traverse the MWNT without scattering. Looking back to the analysis of the number of possible conduction

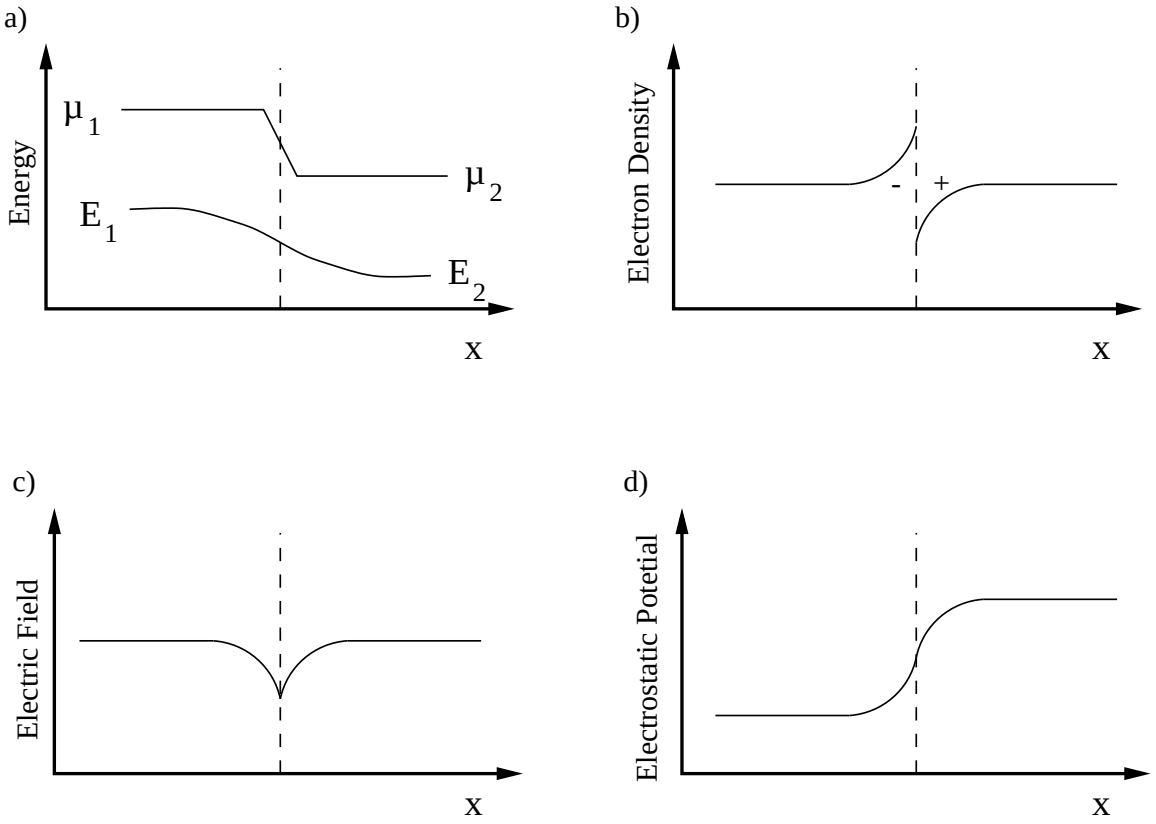

Fig. 4.9. Spatial variation in a) the quasi-Fermi level and the conduction band edge, b) electron density, c) electric field, and d) the electrostatic potential around a single defect. From [4].

modes for a MWNT sample (1 – 112) presented in Chapter 2, this seems to be a low estimate for the number of conduction modes. However as stated earlier, there is no way of determining the number of MWNT shells that are continuous across the gap between contacts.

The inclusion of defects in the nanotube greatly affects how the electrostatic potential is dropped from one contact to the other. As shown in Figure 4.9, a defect may cause a change in the quasi-Fermi level resulting in a charge dipole. An electric field will result from the charge dipole, and there will be a change in the electrostatic potential centered around the defect. The abrupt change in the quasi-Fermi level will be washed out by a distance given by the screening length.

The behavior of the measured electrostatic potential drop down the length of the MWNT will depend on the strength and density of the scatters. Using the convolution model developed in Chapter 3, the effects on the measured electrostatic potential of multiple scatters can be explored. The simulations were designed to model a 100 nm wide MWNT with an overall resistance of 12.8 kΩ, and two current carrying modes. The scattering sites are distributed uniformly across the MWNT, and the MWNT is assumed to be ballistic between scattering sites. The distribution of potential drops is shown in Table 4.1.

Table 4.1
Details of the electrostatic potential drops used in the simulation. $\Delta\phi$ is the electrostatic potential drop located at the contact or the defect. The labels correspond to the labels in Figure 4.10

Number of Defects	$\Delta\phi$ per contact	$\Delta\phi$ per defect (specified)	$\Delta\phi$ per defect (measured)	label
0	210 mV	–	–	a
1	107 mV	206 mV	123 mV	b
2	107 mV	103 mV	65 mV	c
4	107 mV	52 mV	30 mV	d
6	107 mV	34 mV	21 mV	e
8	107 mV	25 mV	13 mV	f

Figure 4.10 shows the result of the simulations. A defect density of two defects per micron will yield a linear drop in the electrostatic potential vs. position profiles. Based on this model, the linear drop associated with Sample 3 may be a result of a small number of scatters present in the MWNT. If this MWNT is ballistic between scatters this MWNT may have mean free paths up to $\sim$ 500 nm.

4.6 Summary

The electrostatic potential of several MWNT samples has been studied with the KFM. Three characteristic behaviors have been seen: i) broken MWNT ropes, ii) a

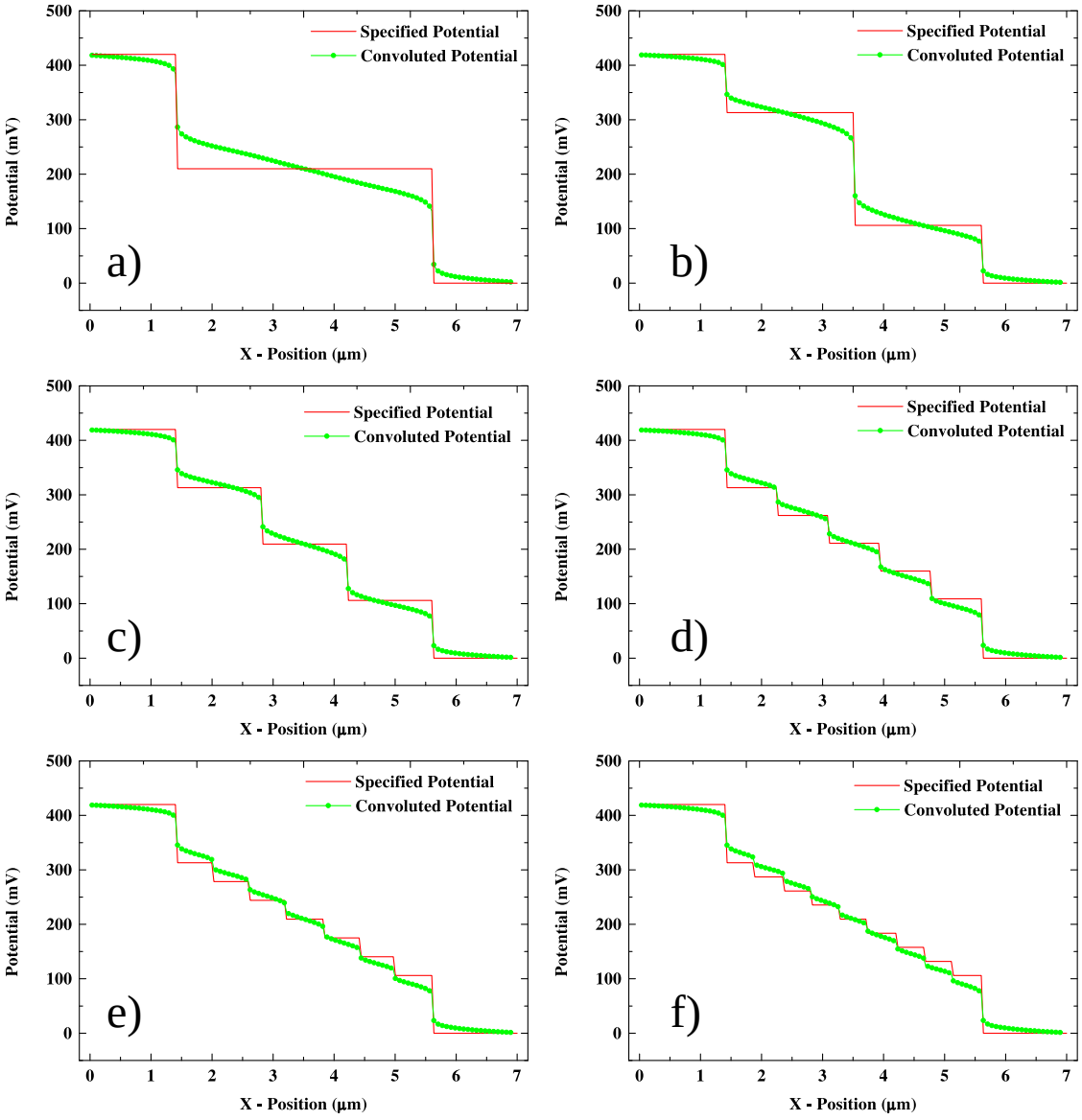

Fig. 4.10. The KFM measurement technique washes out the abrupt potential drop associated with a scatter.

MWNT rope with a localized potential drop corresponding to structural change in the rope, and iii) a MWNT that show a linear potential drop down the length of the rope. The broken MWNT (Sample 1) yields information on the effect of the electrostatic convolution present in the KFM measurement technique. For this MWNT rope, it was seen that there was a significant slope in the electrostatic potential vs. position profile taken over the MWNT. This slope and the results of the simulations performed in Chapter 3 yield an estimate of correction to the measured electrostatic profile that is used in the analysis for Sample 3.

Sample 2 is a MWNT rope that shows a large localized electrostatic potential drop that is correlated to a change in the morphology of the MWNT. The lack of contact resistance may be indicative of diffusive transport or ballistic transport through many conduction channels. However, the large number of broken MWNTs complicate interpretation of the electrostatic potential information.

Sample 3 showed a linear electrostatic potential drop down the length of the MWNT rope with indication of contact resistances of similar magnitude to the resistance of the MWNT. Using information obtained from Sample 1 and the KFM convolution simulations presented in Chapter 3, a correction was applied to the measured electrostatic potential vs. position profile, and MWNT and contact resistances were extracted. The sample resistance was 12.8 kΩ, the measured MWNT resistance is $R_{tube} = 6.1 \pm 0.6$ kΩ, and the contact resistance was measured to be $R_{contact} = 3.4 \pm 0.3$ kΩ per contact. If transport is diffusive, and the current is assumed to be uniformly distributed in the MWNT rope, the conductivity of the MWNT can be found subject to uncertainty in the measurement of the diameter of the MWNT rope. Based on sample dimensions the conductivity of this sample ranged from $\sigma = 1.1^{-7}$ Ω·cm to $\sigma = 1.1^{-9}$ Ω·cm. These values are consistent with conductivities measured for graphitic fibers. However there are questions about the validity of this analysis if the current is not uniformly distributed in the MWNT rope, i. e. current flow through a single MWNT shell. If transport is ballistic, the number of conduction modes can be calculated from the contact resistance. For this sample the number of conduc-

tion modes was estimated to be two. Since the number of modes, and the MWNT resistance is known, the transmission probability can be calculated. For this sample this is calculated to be $T = 0.67 \pm 0.06$. Using the KFM convolution model as developed in Chapter 3, the effect on the electrostatic potential of a varying number of uniformly distributed scatters was investigated. From these simulations, as few as two scattering sites per micron can yield a linearly decreasing electrostatic potential vs. position profile. The electrostatic convolution present in the KFM measurement sets a limit in the minimum measurable mean free path of about 500 nm.

5. POSSIBLE FUTURE WORK

There are both sample and instrumental enhancements possible which may allow this technique to differentiate between the two transport characteristics.

5.1 Sample Considerations

This work was done exclusively on ropes of MWNTs. As seen in the Sample 2, the non–continuous ropes complicate the interpretation of the electrostatic potential images. Interpretation of the KFM data would be much easier if only a single MWNT rope was present in the sample. Work on new methods of placing contacts on nanotubes using a shadow mask technique by Johan Laban may allow contacts to be made to single MWNTs and SWNTs.

Cooling the samples may also distinguish between the two transport mechanisms. Most of the electronic transport measurements are done at low temperatures and low bias to remove thermally and bias activated scatters. It is expected that diffusive and ballistic conductors will have different temperature dependencies. The resistance of a diffusive conductor will decrease due to the reduction in phonon scattering. The electrostatic potential vs. position profiles of ballistic conductors should have no temperature dependence. The primary resistance may be from mode matching between the contacts and the MWNT which is independent of temperature.

5.2 Instrumental Enhancements

Mounting of nanotubes on the ends of AFM tips has been used for several years to increase the lateral resolution of the topography. [10, 56] The cylindrical geometry of these tips can be used to image deep structures. [9] Second, nanotubes can elastically buckle above a critical force. This buckling limits the maximum force applied to a sample, which can prevent damage to delicate organic and biological samples, and makes the tip very robust. Upon first thought, their high aspect ratios should

greatly increase the spatial resolution of the KFM, as well as sample the electrostatic potential more locally yielding a more accurate measurement of $\phi(x, y)$. Using the model developed in Chapter 3, the electrostatic convolution effects of AFM tip with a nanotube mounted on the end can be studied. Figure 5.1 is the nanotube tip used in the following simulations. It models a $\sim 3\mu$m long, 35 nm diameter nanotube mounted onto a tip with a 18° half-angle. As seen in Figure 5.2 and Figure 5.3, there is an improvement in spatial resolution and the accuracy of the measured $\phi(x, y)$. As seen in Figure 5.2, the measured electrostatic potential is 70% of the specified potential as compared to 30% of a standard cantilever. However, the measurement of the electrostatic potential ultimately limited by the effects of the cantilever beam.

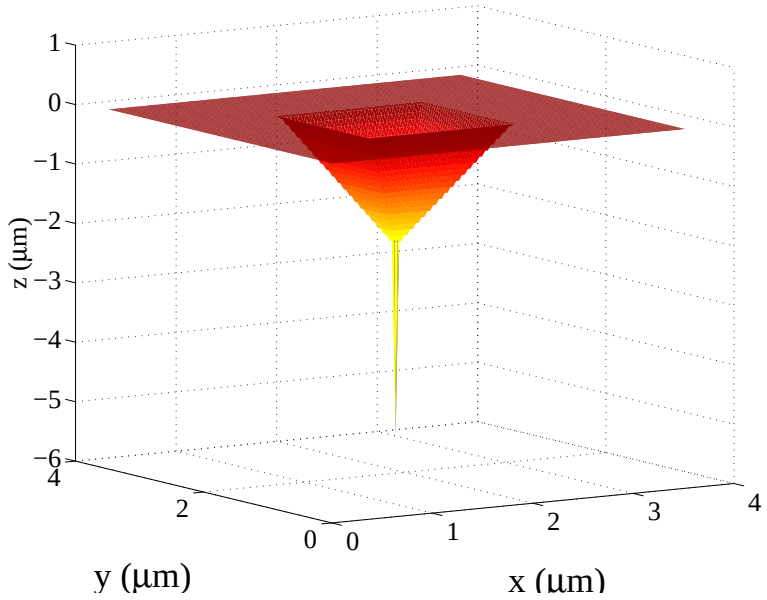

Fig. 5.1. An image of a cantilever with a 18° tip half-angle with a ~ 1 μm flat "ring" that models the cantilever beam. A 3 μm nanotube is mounted on the end of the tip.

Preliminary KFM experiments have been performed using a MWNT rope mounted on the end of the AFM cantilver. A single rope of MWNT was mounted on the end of a standard AFM cantilever. (See Figure 5.4) The method used for mounting the tip is described in detail in the Ph. D Thesis of Michael Buss [50]. Preliminary results

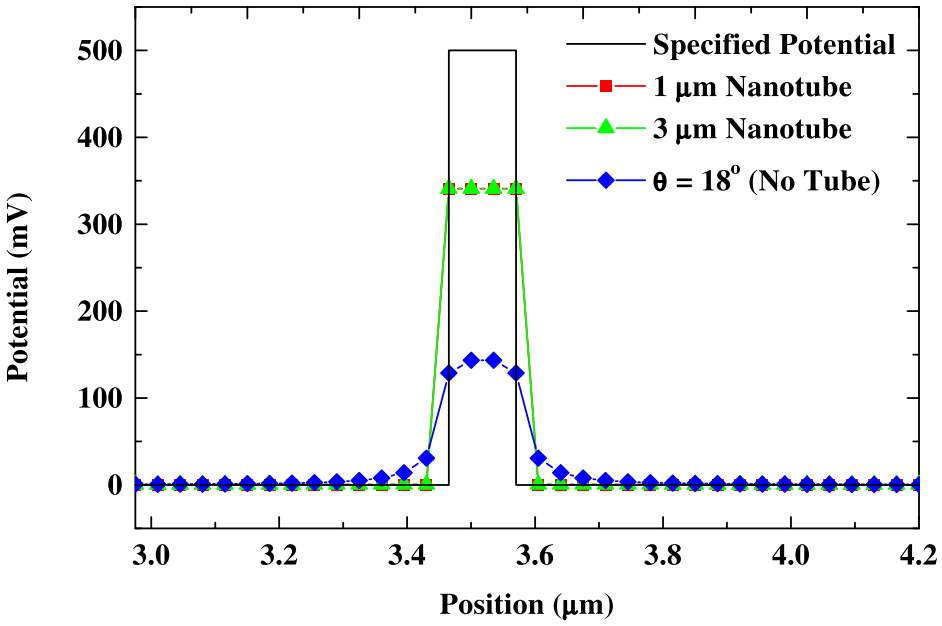

Fig. 5.2. Nanotube tips offer an improvements to the spatial resolution of the KFM measurement. However, the resolution is limited by the effects of the cantilever beam. The electrostatic potential vs. position profiles for the 1 μm long and 3 μm long nanotube tips lie on top of each other.

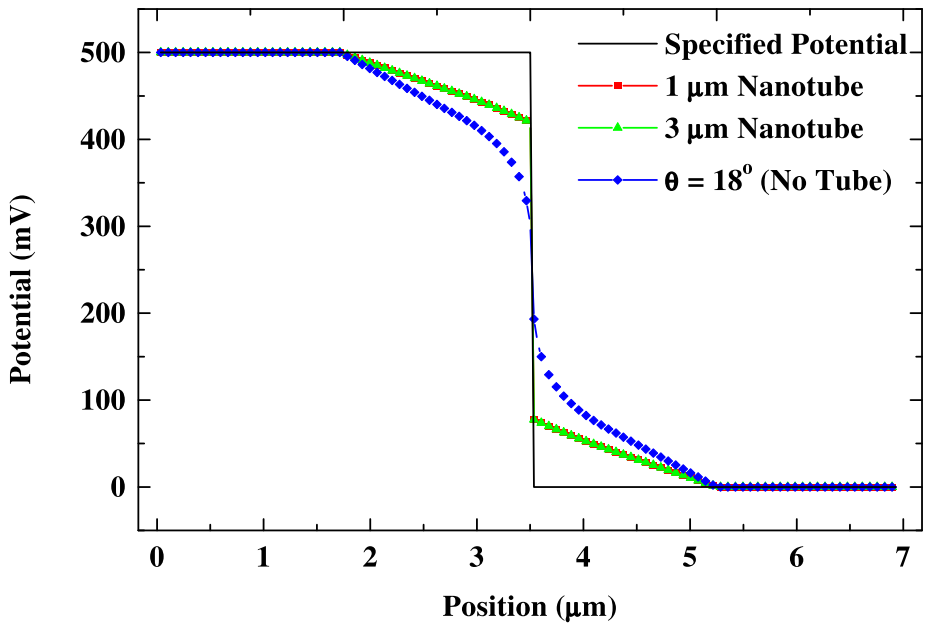

Fig. 5.3. Again the the length of the nanotube does not change the measured electrostatic potential, but both cases are better than a bare AFM tip. The profile for the for the 1 μm and 3 μm nanotube tips lie on top of each other.

indicate that nanotube tips do work as the probe in the KFM measurement, but no significant increase in the spatial resolution of the electrostatic potential measurement can been seen. This may be due to the blunt end form of the nanotube. The measured end radius was $\sim$ 25 nm which is several times larger than the end radius of a new AFM tip. During the measurement of the electrostatic potential, modification of the tip was seen. This is due to the end of the nanotube tip coming into contact with the surface while a large bias is applied. The resulting current flow may have been large enough to break the carbon–carbon bonds at the end of the MWNT.

5.3 KFM Model Improvements

Several enhancements can be made to the program used to model the KFM convolution. The adaptation of this program to use a more accurate method for calculating the capacitance between the tip and the surface is needed if quantative results are required. A balance between the needed accuracy and the speed and complexity of

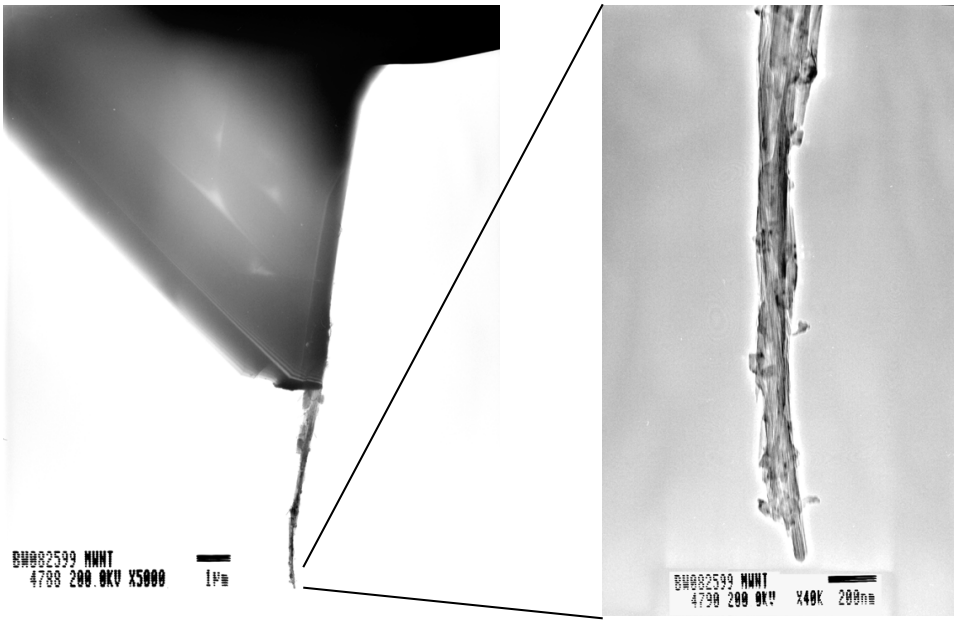

Fig. 5.4. TEM images of a standard AFM cantilever with a ~ 6 μm MWNT mounted on the end. The end radius of the MWNT was ~ 25 nm, which is much larger than the end radii of new AFM tips.

the resulting program must be considered. One possible approach to this problem may be to modify the current convolution program to call on an external program such as Fast-cap to perform the capacitance calculations.

As discussed in Chapter 2, all the simulations presented in this work were on planar (2D) samples. As seen from the topography images presented in Chapter 4, the samples are not planar. As a result, the capacitive coupling between the tip and the surface will be dependent on the geometry of the tip and the geometry of the sample. The program, as written, can be easily modified to simulate a non–planar sample.

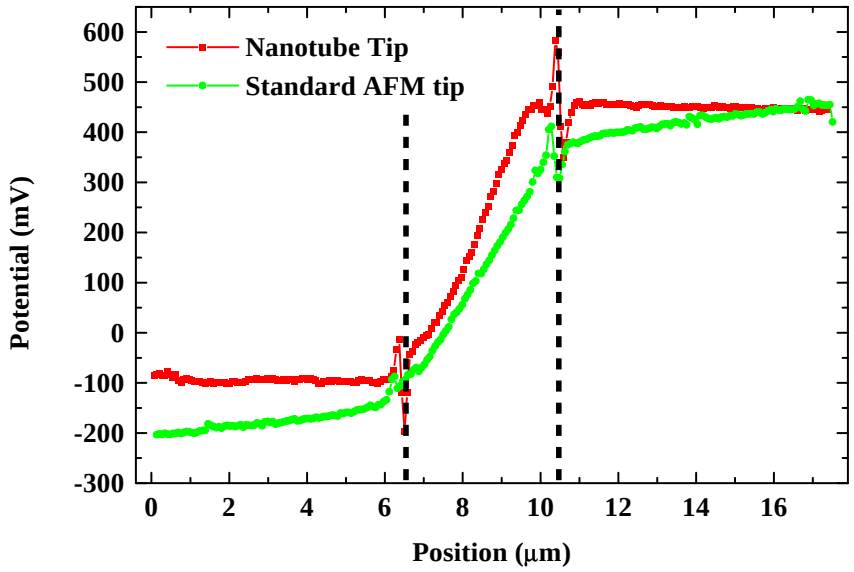

Fig. 5.5. Electrostatic potential vs. position profiles taken well away from the MWNT with both a standard AFM cantilever (green circles) and the nanotube tip (red squares) shown in Figure 5.4. The vertical dashed lines indicate the edges of the contacts.

6. SUMMARY

This work set out to answer the question, are multi-called carbon nanotubes ballistic conductors? In order to answer that question the Kelvin force microscope was used to probe the local electrostatic potential of single ropes of MWNTs. In Chapter 2, the effects on the electrostatic potential from two transport models are considered. If good contacts are assumed, a MWNT whose transport is dominated by diffusive processes will have a linear potential drop between the contacts with the possibility of small potential drops at each contact. This is in contrast to the electrostatic potential profile of an ideal ballistic MWNT which has large electrostatic potential drops at each contact and no potential drop over the MWNT. In Chapter 3, the KFM measurement technique was explained, and a model was developed to understand the convolution of the electrostatic potential present in this measurement technique. This model was demonstrated on several simple test structures. Based on the results of Chapter 2, it is possible to solve Laplace's equation subject to the boundary conditions as dictated by the transport model, and the sample structure. Using the information from the resulting two dimensional electrostatic potential map, the convolution effects of the KFM can be studied. The change in the electrostatic potential vs. position profile resulting from the convolution of the electrostatic potential for the diffusive transport method was minimal. However, for the simulated ideal ballistic MWNT, the convolution of the electrostatic potential resulted in a $\sim 25\%$ slope in the electrostatic potential vs. position profile. However, even with the presence of the electrostatic potential convolution, it is possible to distinguish between the two transport mechanisms.

Using a shadow mask based fabrication technique, low resistance contacts have been placed on the ends of single MWNT ropes. KFM studies of samples prepared

in this manner show three behaviors. i) Sample 1, a broken MWNT, was used to get a rough estimate of the electrostatic potential convolution present in the KFM used in this experiment. For a 100 nm diameter MWNT the correction to the electrostatic potential vs. position curve was about 20%. ii) Sample 2 showed a large localized potential drop located near a change in the morphology of the MWNT rope. The lack of contact resistance may be indicative of diffusive or of many moded ballistic transport in the MWNT rope. iii) Sample 3 displayed a linear potential drop with evidence of contact resistance. The behavior of this MWNT does not distinguish between diffusive and ballistic transport mechanisms. Analysis in the context of diffusive transport yielded values for the conductivity consistent with values found for diffusive transport through carbon fibers. Modeling of the convolution effects on a ballistic MWNT with uniformly distributed scatters results in a linear drop in the electrostatic potential vs. position profile. Based on this transport model, the number of conduction modes, an estimate for the transmission probability, and an estimate for the maximum mean free path was obtained. However, as stated earlier, based on this measurement technique alone, it is not possible to distinguish between diffusive and ballistic transport models in MWNT.

LIST OF REFERENCES

[1] Elton Graugnard. *Preliminary Examination, Purdue University Dept. of Physics*, xx:xx, 1999.

[2] P.J. De Pablo, E. Graugnard, B. Walsh, R.P. Andres, S. Datta, and R. Reifenberger. *Appl. Phys. Lett.*, 74:323, 1999.

[3] E. Graugnard, B. Walsh, P.J. de Pablo, R.P. Andres, S. Datta, and R. Reifenberger. Electronic conductance of multi-walled carbon nanotubes having reliable electrical contacts. In P. Jena, B.K. Rao, and S.N. Khanna, editors, *Cluster and Nanostructured Interfaces*, page xx. Plenum Press, New York, 2000.

[4] S. Datta. *Electronic Transport in Mesoscopic Systems,Cambridge University Press*, B39:1411, 1995.

[5] S. Iijima. *Nature*, 354:56–58, 1991.

[6] J.W. Mintmire, B.I. Dunlap, and C.T. White. *Phys. Rev. Lett.*, 1992:631–634, 1992.

[7] R. Martel, T. Schmidt, H.R. Shea, T. Hertel, and Ph. Avouris. *Appl. Phys. Lett.*, 73:2447–2449, 1998.

[8] H. Dai, N. Franklin, and J. Han. *Appl. Phys. Lett.*, 73:1508–1510, 1998.

[9] G. Nagy, M. Levy, R. Scarmozzino, Jr. R.M. Osgood, H. Dai, R.E. Smalley, C.A. Michaels, G.W. Flynn, and G.F. McLane. *Appl. Phys. Lett.*, 73:529–531, 1998.

[10] H. Dai, J. H. Hafner, A. G. Rinzler, D. T. Colbert, and R. E. Smalley. *Nature*, 384:147–150, 1996.

[11] P.L. McEuen. *Nature*, 393:16, 1998.

[12] R. Egger. *Phys. Rev. Lett.*, 83:5547–5550, 1999.

[13] M. Bockrath, D.H. Cobden, J. Lu, A.G. Rinzler, R.E. Smalley, L. Balents, and P.L. McEuen. *Nature*, 397:598–601, 1999.

[14] C. Kane, L. Balents, and M.P.A. Fisher. *Phys. Rev. Lett.*, 79:5086–5089, 1997.

[15] R. Egger and A.O. Gogolin. *Phys. Rev. Lett.*, 79:5082–5085, 1997.

[16] O.M. Yevtushenko, G.Ya. Slepyan, S.A. Maksimenko, A. Lakhtakia, and D.A. Romanov. *Phys. Rev. Lett.*, 79:1102–1105, 1997.

[17] M.F. Lin, D.S. Chuu, and K.W.-K. Shung. *Phys. Rev. B*, 56:1430–1438, 1997.

[18] P.J. de Pablo, S. Howell, S. Crittenden, B. Walsh, E. Graugnard, and R. Reifenberger. *Appl. Phys. Lett.*, 75:3941–3943, 1999.

[19] A. Bachtold, M. Henny, C. Terrier, C. Strunk, C. Schönenberger, J.-P. Salvetat, J.-M. Bonard, and L. Forró. *App. Phys. Lett.*, 73:274–276, 1998.

[20] S. Frank, P. Poncharel, Z.L. Wang, and W. A. de Heer. *Science*, 20:1744, 1998.

[21] S.J. Tans, M.H. Devoret, H. Dai, A. Thess, R.E. Smalley, L.J. Geerligs, and C. Dekker. *Nature*, 386:474, 1997.

[22] T.W. Ebbesen, H.J. Lezec, H. Hiura, J.W. Bennett, H.F. Ghaemi, and T. Thio. *Nature*, 382:54–56, 1996.

[23] L. Langer, L. Stockman, J.P. Heremans, V. Bayot, C.H. Olk, C. Van Haesendonck, Y. Bruynseraede, and J-P. Issi. *J. Mater. Res.*, 9:927–932, 1994.

[24] M. Dresselhaus. *Science of Fullerenes and Carbon Nanotubes*, page 778, 1996.

[25] A. Oberlin, M. Endo, and T. Koyama. *J. Crystal Growth*, 32:335–349, 1976.

[26] H.W. Kroto, J.R. Heath, S.C. O'Brien, R.F. Curl, and R.E. Smalley. *Nature*, 318:162, 1985.

[27] K. Sattler. *Carbon*, 33:915–920, 1995.

[28] M.S. Dresselhaus, G. Dresselhaus, and P.C. Eklund. *Science of Fullerenes and Carbon Nanotubes*. Academic Press, New York, 1996.

[29] T.W. Ebbesen. *Annu. Rev. Mater. Sci.*, 24:235–264, 1994.

[30] P.R. Wallace. *Phys. Rev.*, 71:622–634, 1947.

[31] P. Delaney, H.J. Choi, J. Ihm, S.G. Louie, and M.L. Cohen. *Nature*, 391:466–468, 1998.

[32] D. L. Carroll, P. Redlich, P. M. Ajayan, J. C. Charlier, X. Blase, A. De Vita, and R. Car. *Phys. Rev. Lett.*, 78:2811–2814, 1997.

[33] R. Tamura and M. Tsukada. *Phys. Rev. B*, 52:6015–6026, 1995.

[34] J.-C. Charlier, T.W. Ebbesen, and Ph. Lambin. *Phys. Rev. B*, 53:11108–11113, 1996.

[35] E.G. Gal'pern, I.V. Stankevich, A.L. Chistyakov, and L.A. Chernozatonskii. *JETP Lett.*, 55:483–486, 1992.

[36] J.W. Mintmire and C.T. White. *Phys. Rev. Lett.*, 81:2506–2509, 1998.

[37] S. Datta. (Private Communication).

[38] C.T. White and J.W. Mintmire. *Nature*, 394:29–30, 1998.

[39] J. C. Charlier and Ph. Lambin. *Phys. Rev.*, B57:R15037–39, 1998.

[40] A. Bachtold, C. Strunk, J-P. Salvetat, J-M. Bonard, L. Forró, T. Nussbaumer, and C. Schönenberger. *Nature*, 397:673–675, 1999.

[41] C. Schönenberger, A. Bachtold, C. Strunk, J.-P. Salvetat, and L. Forró. *Appl. Phys. A*, 69:283–295, 1999.

[42] E. Graugnard, B. Walsh, P. J. de Pablo, A. W. Ghosh, S. Datta, and R. Reifenberger. *PRB Rapid Communications*, xx:xx, 2000.

[43] Lord Kelvin. *Philos. Mag.*, 46:82, 1898.

[44] M. Nonnenmacher, M.P. O'Boyle, and H.K. Wickramasinghe. *Appl. Phys. Let.*, 58:2921, 1991.

[45] O. Vatel and M. Tanimoto. *J. Appl. Phys.*, 77:15, 1995.

[46] H. O. Jacobs, H. F. Knapp, S. Mller, and A. Stemmer. *Ultramicroscopy*, 69:39, 1997.

[47] H. O. Jacobs, H. F. Knapp, and A. Stemmer. *Rev. Sci. Instrum.*, 70:1756, 1999.

[48] H. O. Jacobs, P. Leuchtmann, O. J. Homan, and A. Stemmer. *J. Appl. Phys.*, 84:1168–1173, 1998.

[49] R. Harrington. *Field Computation by Moment Methods.* Macmillian Company, New York NY, 1968.

[50] Mike Buss. *PhD thesis, Chemical Engineering, Purdue University*, 8:67, 1997.

[51] B. Anczykowski, D. Krüger, K.L. Babcock, and H. Fuchs. *Ultramicroscopy*, 66:251–259, 1996.

[52] J. Tamayo and R. García. *Appl. Phys. Lett.*, 71:2394, 1997.

[53] S.N. Magonov, V. Elings, and M.-H. Whangbo. *Surf. Sci.*, 375:385–391, 1997.

[54] Z. Yao, H.W. Ch. Postma, L. Balents, and C. Dekker. *Nature*, 402:273–276, 1999.

[55] M.S. Dresselhaus, G. Dresselhaus, K. Sugihara, I.L. Spain, and H.A. Goldberg. In M. Cardona, editor, *Graphite Fibers and Filaments*, pages 188–202. Springer Series in Materials Science (5), New York, 1988.

[56] S.S. Wong, E. Joselevich, A.T. Woolley, C.L. Cheung, and C.M. Lieber. *Nature*, 394:52–55, 1998.

[57] G. Binnig, H. Rohrer, Ch. Gerber, and E. Weibel. *Phys. Rev. Lett.*, 49:57, 1982.

[58] G. Binnig, C.F. Quate, and Ch. Gerber. *Phys. Rev. Lett.*, 56:930, 1986.

[59] Y. Martin, C.C. Williams, and H.K. Wickramasinghe. *J. Appl. Phys.*, 61:4723, 1987.

[60] D. Sarid, T. G. Ruskell, R. K. Workman, and D. Chen. *J. Vac. Sci. Technol. B*, 14(2):864, 1996.

[61] C. Kittel. *Introduction to Solid State Physics*, page 56, 1996.

[62] Dror Sarid. *Scanning Force Microscopy.* Oxford University Press, 1991.

[63] J. Chen, R. K. Workman, D. Sarid, and R. Hoper. *Nanotechnology*, 5:199–204, 1994.

[64] X. Chen, M. C. Davies, and C. J. Roberts. *Ultramicroscopy*, 75:171–181, 1998.

APPENDIX

With the development of the scanning tunneling microscope (STM) by Gerd Binnig and Heini Rohreer in 1982 [57], a new world of possibilities opened up in the study of materials at the atomic scale. The STM is based on the the phenomenon of the quantum mechanical tunneling of electrons from sharp metallic tip when it is brought sufficiently ($\leq$ 1 nm) close to a metallic surface. While an invaluable tool in surface science, the STM is limited to probing conductive samples. Also, the resulting image of the surface of the material is a convolution of the topographic and electronic state information complicating the interpretation. In 1986, Gerd Binning, Calvin Quate, and Christopher Gerber published the first results from an Atomic Force Microscope (AFM).[58] The AFM relies on the ability to measure forces of less than 1 pN [59], and is not limited to conductive substrates. Because of its unique capabilities, the AFM has seen widespread use in biology, chemistry, material science, physics, and engineering.

A.1 Force Microscopy Principles

The Atomic Force Microscope (AFM) uses a fine tip attached to a flexible cantilever to record the morphology of the surface. (See Figure A.1) In the instrument used in this study (Nanoscope IIIa, Digital Instruments) variations in deflection of the cantilever are sensed using a "beam bounce" technique. A laser is focused onto the back of the cantilever, and a four quadrant photodetector is placed in the path of the light reflected from the back of the cantilever. By recording the differences in the intensity of light striking the individual quadrants of the photodetector, the cantilever's deflection can be monitored. The sample is mounted under the cantilever on top of piezoelectric a scanner capable of motion in the X, Y and Z directions.

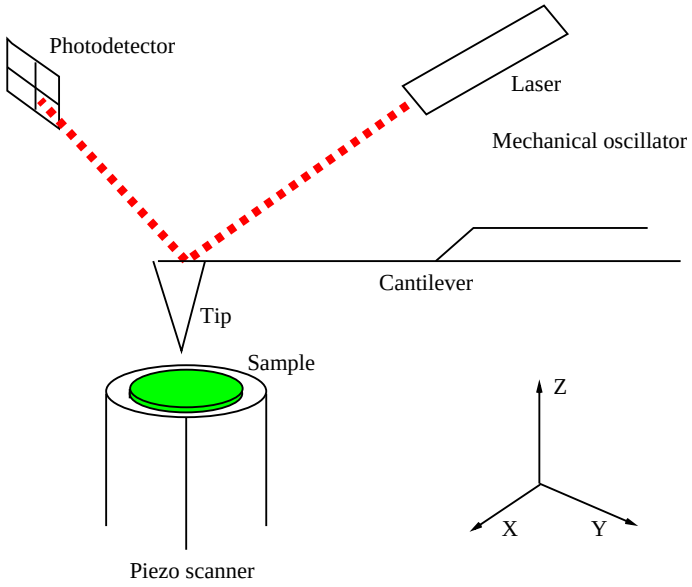

Fig. A.1. Schematic AFM with "beam bounce" detection technique.

A.1.1 Modes of operation

There are three modes of operation in an AFM, contact, non-contact and, intermittent contact (tapping) mode. The choice of mode depends on the sample and the goals of the study. In this study both tapping and non-contact modes were used exclusively. For completeness, all three modes will be discussed. Taking a Lennard–Jones type interaction as shown in Figure A.2 for a sphere-plane system, the force between the tip and sample can be either attractive or repulsive depending on the separation distance.[60, 61] In contact mode AFM, the tip is in "contact" with the sample surface and measures repulsive interatomic forces. In non-contact mode the cantilever is mechanically oscillated near its mechanical resonance frequency a small distance $(20 - 50)$ nm above the surface of the sample. At this distance the tip can be made sensitive to interatomic attractive forces, electrostatic forces, and magnetic forces. In intermittent contact mode, referred to as "tapping" mode from now

on, the cantilever is mechanically oscillated on or near its resonance frequency close enough to the surface to experience the interatomic repulsive forces for a fraction of its oscillation period.

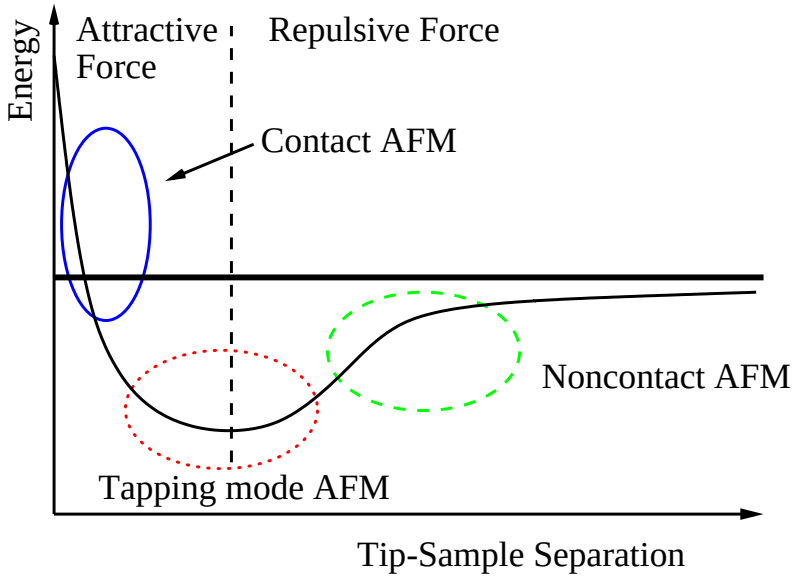

Fig. A.2. Schematic of the interatomic force vs. potential for an undeformed spherical tip and flat substrate.

A.1.2 Contact mode AFM

In contact mode AFM, a cantilever with a very low spring constant $k \leq 0.1\text{N/m}$ is brought into contact with the sample. After the tip is in contact with the sample the deflection of the cantilever is monitored and can be recorded or used as an input to a feedback loop. This feedback loop uses the deflection information to modulate the voltage applied to the Z piezo. The feedback modulates the Z piezo to maintain a constant cantilever defection and therefore a constant cantilever force. The Z piezo is calibrated so for a given applied voltage, the position of the Z piezo is known. Typically the force exerted on the sample is 10^{-6} to 10^{-8} N. This force may be relatively small, but is distributed over a contact area of $\sim 10^{-15}$ nm^2. This will exert a pressure on the sample of $\sim 10^6$ N/m^2. For many applications this will modify the

sample surface. An other consideration is the shear force applied to the surface as the cantilever is rastered in XY. The magnitude of this force more difficult to determine, but is noticeable on many soft samples. However, this method is capable of imaging the atomic corrugation of HOPG and mica in ambient conditions.

A.1.3 Non–contact AFM

In order to probe electric, magnetic, and atomic forces, a cantilever with a spring constant of $k \simeq 1 - 15\text{N/m}$ is oscillated above a sample. The cantilever/beam system can be modeled as a forced–damped simple harmonic oscillator described as [62]

$$m\frac{\partial^2 z}{\partial t^2} + \gamma\frac{\partial z}{\partial t} + k(z-u) = F(z), \tag{A.1}$$

where m is the effective mass of the cantilever, k is the spring constant of the cantilever, γ is a term representing the damping of the cantilever, and u is the position of the cantilever given by $u = u_0 + a\exp(i\omega t)$ where a is the oscillation amplitude of the piezo electric bimorph on which the cantilever is mounted. $F(z)$ is the non-uniform interaction force given by

$$F(z) = F_o(z_o) + \frac{\partial F}{\partial z}\delta, \tag{A.2}$$

where δ is given by $\delta = A_b\exp[i(\omega t - \theta)]$, where A_b is the cantilever oscillation amplitude, and θ is a time independent phase angle. $F(z) = F_o(z_o)$ is the force exerted on the cantilever at a distance z_0 above the surface.

For an oscillation amplitude much less than the tip–sample separation distance, a pertubative approximation can be used to model the influence of the tip–sample force on the mechanical properties of the vibrating cantilever. In this approximation, the solution to Equation A.1 yields an effective spring constant of $k_1 = k + \partial F/\partial z$, and a shifted resonance frequency of $\omega_1 = (k_1/m)^{(1/2)}$ where m is the effective mass of the cantilever. When the cantilever is subject to a positive force gradient, $\partial F/\partial z$ is positive, the effective spring constant increases, and the resonance frequency increases. The opposite effect occurs in the presence of a negative force gradient. The shift in

resonance frequency can be recorded or used as the input to a feedback loop which changes the tip–sample separation to maintain a constant resonance frequency.

Due to the relatively large tip–sample separation, the lateral resolution of an AFM operating non–contact mode is reduced compared to contact or tapping mode. However, the forces exerted by the tip on the sample are very small making the technique very non-invasive.

A.1.4 Tapping mode AFM

Tapping mode offers high lateral resolution similar to contact mode operation with the non–invasiveness of non–contact mode operation. This allows the imaging of soft or delicate samples. Tapping mode is similar to non–contact mode except in that the cantilever is oscillated on or near its resonance frequency , but the tip–sample separation distance is less than the oscillation amplitude so the tip is briefly in contact with the sample. The impact imparts an impulse to the cantilever which shifts the resonance frequency upwards. The shift off resonance is detected as a decrease in oscillation amplitude, which is used by the feedback loop to modulate the tip-sample separation distance voltage in order to maintain a constant oscillation amplitude.

As in the case of non–contact operation, the system can me modeled as a forced–damped harmonic oscillation. However in this case the force experienced by the cantilever is very non–linear, precluding an analytical solution to the differential equation. Numerical simulations have been used to approximate the behavior of the cantilever. [51, 52, 53, 60, 63, 64] The estimated force exerted on the sample ranges from 10^{-7} N to 10^{-9}N which is similar to forces exerted in contact mode AFM. However because the tip is in contact with the sample for only a short period of time, the shear (XY) forces exerted on the sample are much smaller than in contact mode AFM.

This appendix contains the source code to the Laplace equation solver as well as the KFM convolution program.

A.2 Laplace Equation Solver

This version of the program models a ballistic conductor without scattering.

```
// Version 2.0 of laplace solver
// This version will automatically loop until convergence
// criteria is met.
// Also should be be faster relaxing matrix
#include<iostream.h>
#include<stdio.h>
#include<math.h>

#define N 600           // Size of potential array
#define num_iter 1000   // number of iterztions between
                        // tol checks
#define DELM 0.000001   // convergence goal

#define min(a, b)       ((a) < (b) ? (a) : (b))
#define max(a, b)       ((a) < (b) ? (b) : (a))

double pot_arr[N][N]={0.2};  //holds (n-1)th potential array
double pot_arr_2[N][N]={0.2}; // holds nth potential array

void seed_array(void);  // Where to put boundry conditions

FILE *fout;

int main(void)
{
  int i, j, k;
  int counter=0;    // counts total number of iterations
  double del=100;   // record maximum change in voltage per iteration
                    // set high to make sure of 1st iteration

  if ((fout = fopen("ntbal.dat","w")) ==NULL) {
    printf("\nCannot open output file!\n ");
      }

  // initialize potential array
//   for (i=0;i<N;i++) {
```

```
//     for(j=0; j<N;j++){
//       pot_arr[i][j] = 0.0;
//       pot_arr_2[i][j] = 0.0;
//     }
//   }

  // Seed potential array
  cout << "Seeding array" << endl;
  seed_array();

  // relaxation
  cout << "relaxing array" << endl;
  while (del > DELM) {
    for(k=0;k<num_iter;k++){
      if( counter%10000 == 0) {
        cout << "Iteration = " << counter << endl;
      }
      counter++;
      del=0.0; // reset delta V variable
      // Explicitly dealing with the boundries,
      // then calculating internal points
      // Saves 8 if..else statements
      // Memory thrashing problems???

      // Corners first
      pot_arr_2[0][0]=(pot_arr[1][0]+pot_arr[0][1])/2;
      pot_arr_2[0][N-1]=(pot_arr[1][N-1]+pot_arr[0][N-2])/2;
      pot_arr_2[N-1][N-1]=(pot_arr[N-2][N-1]+pot_arr[N-1][N-2])/2;
      pot_arr_2[N-1][0]=(pot_arr[N-2][0]+pot_arr[N-1][1])/2;
      // Assert: no corners

      // Next sides
      for (j=1;j<N-1;j++) {
        pot_arr_2[0][j]=(pot_arr[0][j+1]+pot_arr[0][j-1]+
                         pot_arr[1][j])/3;
        pot_arr_2[N-1][j]=(pot_arr[N-1][j+1]+pot_arr[N-1][j-1]+
                           pot_arr[N-2][j])/3;
      }
      for (i=1;i<N-1;i++) {
        pot_arr_2[i][0]=(pot_arr[i-1][0]+pot_arr[i+1][0]
                         +pot_arr[i][1])/3;
        pot_arr_2[i][N-1]=(pot_arr[i-1][N-1]+pot_arr[i+1][N-1]
                           +pot_arr[i][N-2])/3;
```

```
      }
      // Assert: no side entries

      // Relax internal points
      // bulk of work done here
      for (i=1;i<N-1;i++) {
        for(j=1;j<N-1;j++) {
          pot_arr_2[i][j]=(pot_arr[i][j-1]+pot_arr[i][j+1]+
                           pot_arr[i+1][j]+pot_arr[i-1][j])/4;
        }
      }
      // reseading array
      seed_array();

      // finding max change in potential
      // and copying new array to old array for next iteration
      for (i=0;i<N;i++) {
        for(j=0;j<N;j++){
          del=max(del,fabs(pot_arr[i][j]-pot_arr_2[i][j]));
          pot_arr[i][j] = pot_arr_2[i][j];
        }
      }
    }
    cout << "del=" << del << endl;
  }  // if (del > DELM)

  cout << "Total Iterations " << counter << endl;
  cout << "Writing array" << endl;
  for (i=0;i<N;i++) {
    for(j=0;j<N;j++){
      fprintf(fout,"%d, %d, %g \n",i,j,pot_arr[i][j]);
      //fprintf(fout,"%g\n",pot_arr[i][j]);
    }
  }
  fclose(fout);

}

void seed_array(void)
{
  int i,j;
  for(i=0; i<240; i++) {
    for(j=0; j<600; j++) {
```

```
      pot_arr[i][j] = 0.4;
      pot_arr_2[i][j] = 0.4;
    }
  }

  for(i=360; i<600; i++) {
    for(j=0; j<600; j++) {
      pot_arr[i][j] = 0;
      pot_arr_2[i][j] = 0;
    }
  }
  for(i=240; i<360; i++) {
    for(j=298; j<302; j++) {
      pot_arr[i][j] = 0.2;
      pot_arr_2[i][j] = 0.2 ;
    }
  }


  // pot_arr[50][50] = 1.0; // point source
  //pot_arr_2[50][50] = 1.0;
}
```

A.3 KFM Convolution Program

```
// 03/12/00 copied tarr2.cc to jacobs.cc
// 03/14/00 copied jacobs_tip_beam.cc  tojacobs_tip_beam3d.cc
// Breaking up tip and surface into small parallel plate capactors
// "scanning" tip over surface to see effects on capacitance


// should be independent of length scale.
// including the effects of the cantilever beam in the simulation
// 1 point=35nm scale used for everything.


#include<iostream.h>
#include<stdio.h>
#include<math.h>
```

```
#define EPSA 1    // epsilon0 A
#define HWIDTH 50     // tip half width
// size of array which describes tip
#define TIP_ARR_SIZE HWIDTH+HWIDTH+1
//size of array which describes surface
#define SUR_ARR_SIZE 600
// stores tip geometry
double tip_arr[TIP_ARR_SIZE][TIP_ARR_SIZE]={0};
// stores sample position info
double sur_arr[SUR_ARR_SIZE][SUR_ARR_SIZE]={0};
// store voltage values of surface array
double pot_arr[SUR_ARR_SIZE][SUR_ARR_SIZE]={0};
// capacitance vs position
double cap[SUR_ARR_SIZE][SUR_ARR_SIZE]={0};
// dC/dz vs position
double dCdz[SUR_ARR_SIZE][SUR_ARR_SIZE]={0};
// resulting potential vs position
double pot[SUR_ARR_SIZE][SUR_ARR_SIZE]={0};



int main(int argc, char **argv)
{
  int i,j,k,l,m,tmp_i,tmp_j;    //some handy integers
  int min_index=0;    // integer to hold index of lowest point on tip
  double cap_temp, dCdz_temp=0;
  float tmp_pot;
  int tip_arr_size=TIP_ARR_SIZE;
  int sur_arr_size=SUR_ARR_SIZE;

  int beam_length=29; //half  number of points allocated for beam
  int tip_length=40;   //numper of points allocated for tip
  int bl=beam_length;
  int tl=tip_length;
  FILE *fpotin,*fpotout,*ftipout;

  printf("KFM convolution program.\n");
  if (argc!=4){
    printf("Usage, kfmconv <potinfile> <tipoutfile> <potoutfile>\n");
    exit(1);
  }

  if ((fpotin = fopen(argv[1],"r")) ==NULL) {
```

```
  printf("\nCannot open potential input file!\n ");
}

if ((ftipout = fopen(argv[2],"w")) ==NULL) {
  printf("\nCannot open tip output file!\n ");
}

if ((fpotout = fopen(argv[3],"w")) ==NULL) {
  printf("\nCannot open potential output file!\n ");
}

cout << " Reading in potential array " << endl;
// read in potential from fpotin
for(i=0;i<SUR_ARR_SIZE;i++) {
  for(j=0;j<SUR_ARR_SIZE;j++) {
    fscanf(fpotin,"%d, %d, %g",&tmp_i,&tmp_j,&tmp_pot);
    pot_arr[i][j]=tmp_pot;
    //cout << " pot_arr = " << pot_arr[i][j] << endl;
  }
}

fclose(fpotin);

cout << " Creating tip " << endl;
double height=0.5;   // height above surface

// Define tip geometry
// define tip
//

// define beam everywhere
for(i=0;i<tip_arr_size; i++) {
  for(j=0;j<tip_arr_size; j++) {
    tip_arr[i][j]=height;
  }
}

//define pyramid
k=0;
for (k=0;k<(double)tl/2+1;k++) {
  for (i=0+k;i<=tl-k;i++) {
    for (j=0+k;j<=tl-k;j++) {
      tip_arr[i+bl][j+bl]=-3*k;
```

```
    }
  }
}
// ~3um nanotube 35nm end raidus
// tip_arr[49][49]-=30;

cout << " Writing out tip file " << endl;
//write out tip to file
for(i=0;i<TIP_ARR_SIZE;i++) {
  for(j=0;j<TIP_ARR_SIZE;j++) {
    fprintf(ftipout,"%d, %d, %g \n", i,j,tip_arr[i][j]);
  }
}
fclose(ftipout);

cout << " Convoluting tip " << endl;
// tip convolution section

// Want to calculate capacitance when tip is at constant height over
// sample. Find the point on the tip which is closest to any point
// on the sample and more the tip upwards in the z direction to the
// minimum height raster tip across sample trying to maintain
// minimum separation
for(i=tip_arr_size;i<(sur_arr_size-tip_arr_size); i++) {
  for(j=tip_arr_size;j<(sur_arr_size-tip_arr_size); j++) {

    // find minimum distance in z from tip to surface
    // at given point along the surface, scan across the tip to
    // find the minimum distance from any point on the tip to the
    // corresponding point on the surface. (minimum in Z direction
    // only, not radial!!!!)

    double minimum=100;  // dummy starting point

    for(k=-HWIDTH; k<=HWIDTH; k++) {
      for(l=-HWIDTH; l<=HWIDTH; l++) {
        // at a given point in the surface,
        // step through tip array to find the minimum distance
        // from tip to the surface and record it.
        if((tip_arr[k+HWIDTH][l+HWIDTH]-sur_arr[i+k][j+l])<=minimum){
          // set minimum distance
          minimum=tip_arr[k+HWIDTH][l+HWIDTH]-sur_arr[i+k][j+l];
```

```
        // << " minimum = " << minimum << endl;
        // to minimum distance
      }
      // else do nothing
    }
  }

  if(minimum < height) {
    //cout << " Correting up"  << endl;
    // minimum distance in z is less than height
    // add difference to entire tip
    for(k=0; k<TIP_ARR_SIZE; k++) {
      for(l=0; l<TIP_ARR_SIZE;l++) {
        tip_arr[k][l]=tip_arr[k][l]+(height-minimum);
      }
    }
  }

  if(minimum > height) {
    //cout << " Correcting down " << endl;
    // minimum distance in z is greater or equal to height
    // subtract difference to entire tip (minimum > height)
    for(k=0; k<TIP_ARR_SIZE; k++) {
      for(l=0; l<TIP_ARR_SIZE;l++) {
        tip_arr[k][l]=tip_arr[k][l]-(minimum-height);
      }
    }
  }

// else do nothing

// assuming I have not messed up the tip will be at
// height "height" above sample

// at this constant height, calculate the capacitance
// of each element on the tip and sum up the elements
// to get the total tip/sample capacitance

for(k=-HWIDTH; k<=HWIDTH; k++) {
  for(l=-HWIDTH; l<=HWIDTH; l++) {
  // calculate capacitance
  cap_temp=EPSA/(tip_arr[k+HWIDTH][l+HWIDTH]-sur_arr[i+k][j+l]);
  // dC/dz
```

```
      dCdz_temp=-EPSA/((tip_arr[k+HWIDTH][l+HWIDTH]-sur_arr[i+k][j+l])*
                      (tip_arr[k+HWIDTH][l+HWIDTH]-sur_arr[i+k][j+l]));
      // summing over tip
      dCdz[i][j]+=dCdz_temp;

      // potential wieghting
      pot[i][j]+=pot_arr[i+k][j+l]*dCdz_temp;
      }
    }

    // write out position, capacitance, dCdz, tip position,
    //
    fprintf(fpotout,"%d, %d, %g \n", i,j,pot[i][j]/dCdz[i][j]);
    }
    cout << "i = "<< i << endl;
  }
  fclose(fpotout);
}
```